


Identification of Different Types of High-Frequency Defects in Superconducting Qubits

Leonid V. Abdurakhimov^{1,*}, Imran Mahboob¹, Hiraku Toida¹, Kosuke Kakuyanagi¹,
Yuichiro Matsuzaki² and Shiro Saito^{1,†}

¹NTT Basic Research Laboratories, NTT Corporation, 3-1 Morinosato-Wakamiya, Atsugi, Kanagawa 243-0198, Japan

²Research Center for Emerging Computing Technologies, National Institute of Advanced Industrial Science and Technology (AIST), 1-1-1 Umezono, Tsukuba, Ibaraki 305-8568, Japan

 (Received 10 December 2021; revised 7 October 2022; accepted 1 December 2022; published 21 December 2022)

Parasitic two-level-system (TLS) defects are one of the major factors limiting the coherence times of superconducting qubits. Although there has been significant progress in characterizing basic parameters of TLS defects, exact mechanisms of interactions between a qubit and various types of TLS defects remained largely unexplored due to the lack of experimental techniques able to probe the form of qubit-defect couplings. Here we present an experimental method of TLS defect spectroscopy using a strong qubit drive that allowed us to distinguish between various types of qubit-defect interactions. By applying this method to a capacitively shunted flux qubit, we detected a rare type of TLS defect with a nonlinear qubit-defect coupling due to critical-current fluctuations, as well as conventional TLS defects with a linear coupling to the qubit caused by charge fluctuations. The presented approach could become the routine method for high-frequency defect inspection and quality control in superconducting qubit fabrication, providing essential feedback for fabrication process optimization. The reported method is a powerful tool to uniquely identify the type of noise fluctuations caused by TLS defects, enabling the development of realistic noise models relevant to noisy intermediate-scale quantum computing and fault-tolerant quantum control.

DOI: [10.1103/PRXQuantum.3.040332](https://doi.org/10.1103/PRXQuantum.3.040332)

I. INTRODUCTION

Reducing gate error rates of a physical qubit is one of the biggest challenges on the road to building a gate-based fault-tolerant superconducting quantum computer [1]. For the typical physical error rate of 10^{-3} , a logical qubit would need to contain about 10^3 – 10^4 physical qubits in order to achieve sufficiently low logical error rates [2], and a full-scale realization of quantum applications would require more than 10^7 physical qubits using the standard surface-code approach [3] (this requirement can be slightly relaxed by using hybrid architectures [4]). Potentially, useful tasks can be performed using a noisy intermediate-scale quantum (NISQ) processor consisting of tens to hundreds of physical qubits [5,6], but, even in this case, quantum error mitigation is crucial [7,8]. The

value of a gate error rate can be estimated as the ratio of a gate duration time and a qubit coherence time, and significant efforts have been made to improve gate speeds and qubit coherence. Two-qubit gate error rates of the order of 10^{-3} were demonstrated for transmon qubits with coherence times exceeding $100 \mu\text{s}$ [9]. Possibilities for further improvement of coherence times were demonstrated using novel qubit designs, such as a fluxonium qubit [10,11], a $0-\pi$ qubit [12], and bosonic qubits [13,14]. However, independent of a particular qubit architecture, coherence times are ultimately limited by intrinsic losses in materials constituting a qubit, and reducing the number of material defects is a crucial factor for qubit performance improvement [15–17].

Extensive studies in recent decades have identified major noise sources in superconducting qubits, including parasitic two-level-system (TLS) defects [18–33], quasi-particle noise [34–44], and, for flux-tunable qubits, a $1/f$ magnetic flux noise [45,46]. In this paper, we focus on TLS defects: defects of different microscopic nature that can be modeled as two-level quantum systems, such as tunneling atoms, dangling electronic bonds, impurity atoms, and trapped charge states [27]. TLS defects are ubiquitous in the current generation of superconducting qubits: in the most commonly used method of Josephson

*leonid.abdurakhimov@meetiqm.com

†shiro.saito.bx@hco.ntt.co.jp

‡Present address: IQM Finland Oy, Espoo 02150, Finland.

Published by the American Physical Society under the terms of the [Creative Commons Attribution 4.0 International](https://creativecommons.org/licenses/by/4.0/) license. Further distribution of this work must maintain attribution to the author(s) and the published article's title, journal citation, and DOI.

junction fabrication, a junction tunnel barrier is formed of an amorphous layer of aluminum oxide that hosts a large number of TLS defects [27,33]. Besides, the microwave absorption due to TLS defects formed in various oxide layers is one of the major mechanisms limiting Q factors of microwave superconducting resonators [47,48], including superconducting three-dimensional (3D) cavities that are used for quantum memory applications and bosonic quantum computing [49–51]. Normally, it is assumed that the qubit-defect interaction is caused by an electric field coupling between an electric dipole associated with a charge TLS defect and a microwave electric field generated across a Josephson junction [19].

The standard techniques to study high-frequency TLS defects in superconducting qubits are based on matching the frequencies of qubit and defect transitions in the laboratory frame by either adjusting the qubit frequency with an applied magnetic flux [18,19,21,23,52,53], or changing the defect frequency with an external electrical field or an applied mechanical strain [22,29–31]. Parameters of a TLS defect are then extracted from the splitting of an avoided crossing observed in the qubit spectrum [18,19], the qubit response to a Rabi drive [52,54], or measurements of energy-relaxation times T_1 [23,25,26,29–31]. The standard methods of TLS defect spectroscopy based on the qubit frequency tuning are not suitable for fixed-frequency qubits, such as fixed-frequency transmons. Recently, it was shown that TLS defects in fixed-frequency transmons could be probed by utilizing an ac Stark shift of the qubit frequency induced by an *off-resonant* microwave drive [55]. However, the frequency band of the demonstrated technique was quite narrow (± 25 MHz). Importantly, previously described methods allowed one to study basic parameters of TLS defects, but the exact mechanisms of qubit-defect interactions have remained largely unexplored so far.

In this paper, we describe a method for the identification of different types of high-frequency TLS defects using a strong *resonant* qubit drive. Our approach is based on the notion that the relaxation of a strongly driven qubit can be affected by the presence of an off-resonant high-frequency TLS defect due to the dynamic splitting of the qubit transition frequency, caused by the *resonant* ac Stark effect (Autler-Townes splitting), and the corresponding dynamic matching of qubit and TLS defect frequencies in the rotating frame [56]. In the case of a flux-tunable qubit, the reported technique allows one to extract detailed information about the qubit-defect interaction, including the type of the qubit-defect coupling. We demonstrate the capabilities of the method by performing TLS defect spectroscopy in a capacitively shunted (c-shunt) flux qubit in a wide frequency band ± 120 MHz. By measuring the strongly driven qubit state relaxation at different values of an external magnetic flux bias, we identify two different

types of defects: standard charge-fluctuation TLS defects and TLS defects with a nonlinear coupling to the qubit mediated by critical-current fluctuations.

We show that, near the optimal magnetic flux bias point, the coupling between the qubit and a charge-fluctuation TLS defect has the form of a beam-splitter-type interaction, while a critical-current-fluctuation TLS defect is coupled to the qubit via a three-wave-mixing interaction term. Because of the different shapes of qubit-defect interactions, the dependence of the position of a charge-fluctuation TLS signature on the applied magnetic flux is determined by the corresponding shift of the qubit frequency, while the signature of a critical-current TLS defect follows the double value of the qubit frequency shift. This behavior forms the basis of the reported differentiation technique. In addition, by repeating the measurements with an applied in-plane magnetic field, we can exclude the possibility that observed TLS signatures are caused by magnetic TLS defects.

The reported method of high-frequency defect sensing complements the techniques for the detection of low-frequency TLS defects utilizing a spin-locking pulse sequence [57]. The key difference between those two approaches is that the reported method effectively probes a high-frequency transverse noise, while low-frequency spin-locking spectroscopy methods focus on a low-frequency longitudinal noise [56].

In order to use the described approach for the identification of high-frequency TLS defects in fixed-frequency qubits, such as transmons, one can tune the qubit frequency by applying an in-plane magnetic field [58–61] or by inducing an ac Stark shift using an off-resonant microwave drive [55,62]. If the qubit frequency tunability is completely unavailable, the reported technique cannot be used for the identification of a qubit-defect interaction type, but it can be applied to extract basic parameters of off-resonant TLS defects, including effective qubit-defect frequency detuning and the coupling strength.

Our results also imply that the always-on transverse coupling between a qubit and a high-frequency off-resonant TLS defect would coherently mix bare states of the coupled system. Even when the qubit and TLS defect are detuned, the time evolution of the qubit bare-state population would be characterized by fast small-amplitude oscillations, since the proper eigenstates of the hybrid system are not the bare states, but the qubit-defect entangled states. Those population oscillations due to the nonresonant (dispersive) interaction between the qubit and detuned TLS defects can result in additional gate and measurement errors [63–65]. The importance of the reported method of TLS defect spectroscopy is that it allows one to map off-resonant TLS defects in a wide frequency band, and to extract defect parameters that can be used for numerical gate optimization.

II. THEORETICAL MODEL

In this section, we present a theoretical model of the hybrid system composed of a high-frequency TLS defect and a qubit under a strong microwave drive. Here, a c-shunt flux qubit (CSFQ) is modeled as a nonlinear Duffing oscillator similar to a transmon qubit. We derive qubit-defect interaction terms for different types of TLS defects and show that the shape of the interaction term determines the condition of the dynamical coupling between a qubit and an off-resonant TLS defect.

A. Qubit and TLS defect Hamiltonians

We consider a c-shunt flux qubit consisting of a superconducting loop interrupted by three Josephson junctions shunted by a large capacitance C_S [66–69]. Two junctions are identical and characterized by the same critical current I_c and capacitance C_J , while the area of the third junction is reduced by a factor of α . The large shunt capacitance $C_S \gg C_J$ is connected in parallel with the smaller junction. In this case, the qubit Hamiltonian can be written in the one-dimensional form [67–69]

$$\hat{H}_{\text{CSFQ}} = E_{C_S} \hat{n}^2 + 2E_J(1 - \cos \hat{\varphi}) + \alpha E_J \left[1 - \cos \left(2\pi \frac{\Phi_e}{\Phi_0} + 2\hat{\varphi} \right) \right], \quad (1)$$

where $E_{C_S} \approx e^2/2C_S$ is the effective charging energy, $E_J = \Phi_0 I_c / 2\pi$ is the Josephson energy, $\hat{\varphi}$ and $\hat{n} = -i\partial/\partial\hat{\varphi}$ are phase and Cooper-pair number operators, respectively, Φ_e is an external magnetic flux, and Φ_0 is a magnetic flux quantum. The effective charging energy E_{C_S} is much smaller than the characteristic junction charging energy $E_C = e^2/2C_J$.

By taking into account charge and critical-current noise fluctuations relevant for the smaller Josephson junction (later it will be shown that those fluctuations are related to TLS defects located in this junction), the qubit Hamiltonian close to the optimal magnetic flux bias of $\Phi_e = 0.5\Phi_0$ (“sweet spot”) can be written as

$$\hat{H}_{\text{CSFQ}} = E_{C_S}(\hat{n} + \delta n)^2 + 2E_J(1 - \cos \hat{\varphi}) + \alpha E_J \left(1 + \frac{\delta I_\alpha}{\alpha I_c} \right) [1 + \cos(2\hat{\varphi} + 2\pi \delta f)], \quad (2)$$

where δn is the difference between electric charge fluctuations (in units of $2e$) on the two superconducting islands separated by the smaller Josephson junction [66], δI_α is the fluctuation of the critical current through that junction, and $\delta f = (\Phi_e/\Phi_0) - 0.5$ is the relative flux detuning from the optimal magnetic flux bias.

The potential energy of the c-shunt flux qubit is determined by the second and third terms on the right-hand side of Eq. (2). In the case of $\alpha < 0.5$, the qubit has a

single-well potential similar to a transmon qubit [70]. By expanding cosines for small angles and neglecting noise contributions, the qubit at the optimal magnetic flux bias can be treated as a quantum harmonic oscillator with a fourth-order perturbation term, and the Hamiltonian can be written in the form of a Duffing oscillator [68,69]:

$$\hat{H}_q = \hbar\omega_b \left(\hat{b}^\dagger \hat{b} + \frac{1}{2} \right) + \frac{\hbar A}{12} (\hat{b}^\dagger + \hat{b})^4. \quad (3)$$

Here ω_b is the characteristic frequency of the Duffing oscillator given by

$$\hbar\omega_b = \sqrt{4E_{C_S} E_J (1 - 2\alpha)}, \quad (4)$$

A is the qubit anharmonicity given by

$$\hbar A = \frac{8\alpha - 1}{4(1 - 2\alpha)} E_{C_S}, \quad (5)$$

and \hat{b}^\dagger and \hat{b} are creation and annihilation bosonic operators that are related to the charge and phase operators by

$$\hat{n} = \frac{i}{\sqrt{2}} \left[\frac{E_J(1 - 2\alpha)}{E_{C_S}} \right]^{1/4} (\hat{b}^\dagger - \hat{b}) \quad (6)$$

and

$$\hat{\varphi} = \frac{1}{\sqrt{2}} \left[\frac{E_{C_S}}{E_J(1 - 2\alpha)} \right]^{1/4} (\hat{b}^\dagger + \hat{b}). \quad (7)$$

Using the commutation relation $[\hat{b}, \hat{b}^\dagger] = 1$ and neglecting off-diagonal terms in Eq. (3) (these terms disappear under the rotating-wave approximation used below), the qubit Hamiltonian can be written as

$$\hat{H}_Q = \left(\hbar\omega_b + \frac{\hbar A}{2} \right) \hat{b}^\dagger \hat{b} + \frac{\hbar A}{2} (\hat{b}^\dagger \hat{b})^2 \quad (8)$$

with the frequencies of the two lowest qubit transitions given by

$$\omega_q \equiv \omega_{01} = \omega_b + A \quad (9)$$

and

$$\omega_{12} = \omega_b + 2A. \quad (10)$$

It can be seen from Eq. (8) that, for a typical case when the qubit operational space is limited to the lowest two or three levels, the described perturbation approach should provide meaningful results when the condition $A \ll \omega_b$ is fulfilled.

The Hamiltonian of the TLS defect in the eigenstate basis is given by

$$\hat{H}_{\text{TLS}} = \frac{1}{2}\hbar\omega_{\text{TLS}}\hat{\sigma}_z, \quad (11)$$

where ω_{TLS} is the TLS defect frequency and $\hat{\sigma}_z$ is the Pauli operator of the defect (details can be found in Appendix A).

B. Qubit-defect interaction

The form of the qubit-defect interaction term H_{int} depends on a particular microscopic mechanism of the coupling between a qubit and a TLS defect [27]. In the most commonly used model, it is assumed that a charge TLS defect induces the charge fluctuations δn_{TLS} across a relevant Josephson junction [19,27], and the corresponding interaction Hamiltonian can be obtained by substituting $\delta n = \frac{1}{2}\delta n_{\text{TLS}}\hat{\sigma}_x$ into Eq. (2):

$$\hat{H}_{\text{int}}^{(C)} = i\hbar g_C \hat{\sigma}_x (\hat{b}^\dagger - \hat{b}). \quad (12)$$

Here $\hat{\sigma}_x$ is the Pauli operator of the TLS defect, and g_C is the coupling strength between the qubit and defect given by

$$g_C = \frac{1}{2}\delta n_{\text{TLS}} \sqrt{\frac{\omega_b E_C S}{\hbar}}. \quad (13)$$

According to Eq. (12), the coupling between a qubit and a standard charge TLS defect is linear in terms of the qubit operators \hat{b}^\dagger and \hat{b} .

Another possible interaction mechanism between a qubit and a TLS defect is related to critical-current fluctuations across a Josephson junction [18,27]. Since the thickness of the junction tunnel barrier is nonuniform, the tunneling of Cooper pairs occurs through a discrete set of conductance channels. Fluctuations in the charge configuration of a TLS defect can block one of the conductance channels, resulting in the fluctuations of the critical current δI_{TLS} through that junction [27]. Other possible microscopic models of critical-current noise include Andreev fluctuators [71,72] and Kondo-like traps [73]. The interaction Hamiltonian due to critical-current fluctuations can be estimated by substituting $\delta I_\alpha = \frac{1}{2}\delta I_{\text{TLS}}\hat{\sigma}_x$ into Eq. (2). By expanding the cosine term $\cos(2\hat{\varphi} + 2\pi\delta f)$ for the small phase $\hat{\varphi}$ and flux detuning δf , the interaction term can be written in terms of qubit operators \hat{b}^\dagger and \hat{b} as

$$\hat{H}_{\text{int}} = \hbar g_I^{(1)} \hat{\sigma}_x (\hat{b}^\dagger + \hat{b}) + \hbar g_I^{(2)} \hat{\sigma}_x (\hat{b}^\dagger - \hat{b})^2, \quad (14)$$

where coupling strengths $g_I^{(1)}$ and $g_I^{(2)}$ are given by

$$g_I^{(1)} = -\pi\delta f \frac{\alpha}{\sqrt{1-2\alpha}} \left(\frac{\delta I_{\text{TLS}}}{\alpha I_C} \right) \sqrt{\frac{\omega_b E_J}{\hbar}} \quad (15)$$

and

$$g_I^{(2)} = -\frac{\alpha}{4(1-2\alpha)} \left(\frac{\delta I_{\text{TLS}}}{\alpha I_C} \right) \omega_b. \quad (16)$$

In this work, it is assumed that the qubit is operated close to the optimal flux bias point ($\delta f \approx 0$), and, hence, the interaction between the qubit and TLS defect through critical-current fluctuations is described by the nonlinear term given by

$$\hat{H}_{\text{int}}^{(I)} = \hbar g_I^{(2)} \hat{\sigma}_x (\hat{b}^\dagger + \hat{b})^2. \quad (17)$$

C. Qubit-defect system under a strong drive: linear coupling

First, we consider the driven evolution of the qubit coupled to a standard charge TLS defect. We assume that there is some detuning between the qubit and defect frequencies as shown in Fig. 1(a). The system Hamiltonian is given by

$$\hat{H} = \hat{H}_Q + \hat{H}_{\text{TLS}} + \hat{H}_{\text{int}}^{(C)} + \hat{H}_d. \quad (18)$$

The driving term \hat{H}_d is given by

$$\hat{H}_d = i\hbar\Omega \cos(\omega_q t) (\hat{b}^\dagger - \hat{b}), \quad (19)$$

where Ω is the Rabi angular frequency. Here, it is assumed that the qubit is capacitively coupled to a readout cavity mode via the charge degree of freedom, and the microwave drive is applied at the qubit resonance frequency.

Using the rotating-wave approximation (RWA) (details can be found in Appendix B), the system Hamiltonian in the rotating frame is given by

$$\begin{aligned} \hat{H}^R = & \frac{\hbar A}{2} [(\hat{b}^\dagger \hat{b})^2 - \hat{b}^\dagger \hat{b}] + i \frac{\hbar \Omega}{2} (\hat{b}^\dagger - \hat{b}) + \frac{\hbar \Delta_L}{2} \hat{\sigma}_z \\ & + i\hbar g_C (\hat{b}^\dagger \hat{\sigma}_- - \hat{b} \hat{\sigma}_+), \end{aligned} \quad (20)$$

where $\hat{\sigma}_\pm = \frac{1}{2}(\hat{\sigma}_x \pm i\hat{\sigma}_y)$, and the separation between defect energy levels Δ_L is given by

$$\Delta_L = \omega_{\text{TLS}} - \omega_q. \quad (21)$$

By truncating the qubit state space to the lowest two states, the qubit eigenstate basis for the noninteracting part of the Hamiltonian in the rotating frame is given by

$$|i-\rangle = \frac{|0\rangle - i|1\rangle}{\sqrt{2}} \quad (22)$$

and

$$|i+\rangle = \frac{|0\rangle + i|1\rangle}{\sqrt{2}}. \quad (23)$$

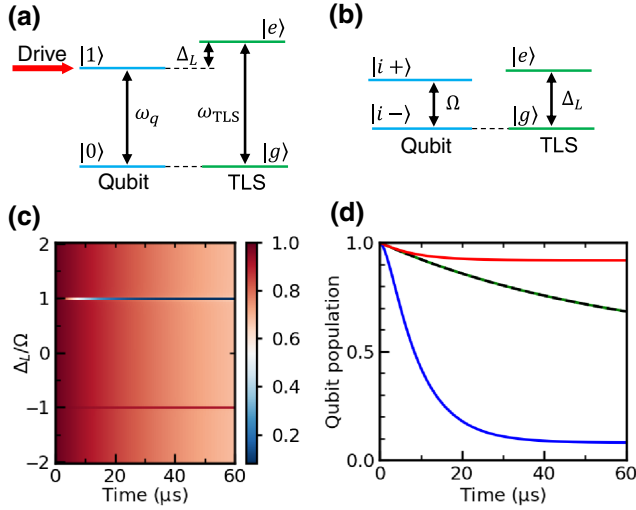


FIG. 1. (a),(b) Energy level diagrams of a qubit and an off-resonant charge-fluctuation TLS defect in the (a) laboratory frame and (b) rotating frame for $\Delta_L > 0$. (c),(d) Results of numerical simulations of the system evolution for a given Rabi frequency. (c) Population of the excited qubit state $|i+\rangle$ in the rotating frame as a function of the evolution time and qubit-defect detuning. The qubit is dynamically coupled to the defect when the condition given by Eq. (25) is met. (d) Qubit population at the qubit-defect detunings $\Delta_L = \Omega$ (blue line), $\Delta_L = -\Omega$ (red line), and $\Delta_L \neq \pm\Omega$ (green line). The dashed black line corresponds to the exponential decay $f(t) = [1 + \exp(-\Gamma_{1q}t/2)]/2$.

In the $\{|i-\rangle, |i+\rangle\}$ eigenstate basis, the system Hamiltonian is given by

$$\hat{H}^R = -\frac{\hbar\Omega}{2}\hat{s}_z + \frac{\hbar\Delta_L}{2}\hat{\sigma}_z - \frac{\hbar g_C}{2}(\hat{s}_z\hat{\sigma}_x + \hat{s}_y\hat{\sigma}_y), \quad (24)$$

where $\hat{s}_{x,y,z}$ are the qubit Pauli operators. By performing a second RWA transformation, it can be shown that the interaction term proportional to $\hat{s}_z\hat{\sigma}_x$ can be neglected, and, hence, the effective coupling strength is equal to $g_C/2$. The diagram of energy levels of the qubit and defect in the rotating frame is shown in Fig. 1(b).

We perform numerical simulations of the system evolution by solving a Lindblad master equation for Hamiltonian (24) in the QuTiP package [74,75] [Figs. 1(c) and 1(d)]. The collapse operators are chosen in the forms $\hat{C}_1 = \sqrt{\Gamma_{1q}}\hat{b} = \sqrt{\Gamma_{1q}}(-\hat{s}_y - i\hat{s}_z)/2$ and $\hat{C}_2 = \sqrt{\Gamma_{1\text{TLS}}}\hat{\sigma}_-$. Here, the qubit pure dephasing is not taken into account, since, for sufficiently high Rabi frequencies, the driven qubit state should be effectively decoupled from low-frequency dephasing noises such as a $1/f$ phase noise [56]. The qubit is initialized in its excited state $|i+\rangle$ in the rotating frame, and the defect is initialized in its ground state $|g\rangle$. The simulation parameters are $\Omega/2\pi = 25$ MHz, $g_C/2\pi = 50$ kHz, $\Gamma_{1q} = 0.03 \mu\text{s}^{-1}$, and $\Gamma_{1\text{TLS}} = 1 \mu\text{s}^{-1}$.

The condition for the dynamical coupling between a qubit and a defect with a linear coupling to the qubit is

given by

$$\Omega = |\Delta_L| = |\omega_{\text{TLS}} - \omega_q|. \quad (25)$$

If the driven qubit state is not coupled to the defect, i.e., $\Omega \neq |\Delta_L|$, the qubit relaxation rate in the rotating frame is given by $\Gamma_{1\rho} = \Gamma_{1q}/2$ [Fig. 1(d)]. When condition (25) is fulfilled, the relaxation of the driven qubit state is affected by the interaction with the defect, and, in the case $\Gamma_{1q} < g_C < \Gamma_{1\text{TLS}}$, the effective relaxation rate of the qubit can be roughly estimated by a Purcell-like formula, $\Gamma_P \approx g_C^2/\Gamma_{1\text{TLS}}$ [56]. The sign of the offset of the stationary qubit population level from the value of 0.5 depends on the sign of the qubit-defect detuning Δ_L [Fig. 1(d)], and, hence, one can say that spectral signatures for defects with negative and positive detunings have different “polarities.” Depending on the “polarity” (i.e., the sign of the detuning Δ_L), a TLS defect can be considered as a “cold” or a “hot” subsystem [56]. When the condition $\Delta_L > 0$ is fulfilled, the ground state of the TLS defect in the laboratory frame corresponds to the ground state in the rotating frame [Fig. 1(b)], and the population is transferred from the qubit to the “cold” TLS defect. In contrast, when the condition $\Delta_L < 0$ is met, the ground state of the TLS defect in the laboratory frame corresponds to the excited state in the rotating frame, and the population is transferred from the “hot” TLS defect to the qubit (details can be found in Appendix C).

D. Qubit-defect system under a strong drive: nonlinear coupling

In this section, we consider the driven evolution of the qubit coupled to a critical-current-fluctuation TLS defect. The system Hamiltonian is given by

$$\hat{H} = \hat{H}_Q + \hat{H}_{\text{TLS}} + \hat{H}_{\text{int}}^{(I)} + \hat{H}_d. \quad (26)$$

By using the RWA (details can be found in Appendix B), the Hamiltonian can be written in the rotating frame as

$$\begin{aligned} \hat{H}^R = & \frac{\hbar A}{2}[(\hat{b}^\dagger\hat{b})^2 - \hat{b}^\dagger\hat{b}] + i\frac{\hbar\Omega}{2}(\hat{b}^\dagger - \hat{b}) + \frac{\hbar\Delta_{\text{NL}}}{2}\hat{\sigma}_z \\ & + \hbar g_I^{(2)}(\hat{b}^{\dagger 2}\hat{\sigma}_- + \hat{b}^2\hat{\sigma}_+), \end{aligned} \quad (27)$$

where the detuning is defined as

$$\Delta_{\text{NL}} = \omega_{\text{TLS}} - 2\omega_q. \quad (28)$$

We perform numerical simulations of the system evolution by solving the master equation for Hamiltonian (27). The qubit states are truncated to the lowest three levels. The collapse operators are $\hat{C}_1 = \sqrt{\Gamma_{1q}}\hat{b}$ and $\hat{C}_2 = \sqrt{\Gamma_{1\text{TLS}}}\hat{\sigma}_-$. The qubit is initialized in its excited state $|i+\rangle$ in the rotating frame, and the defect is initialized in its ground

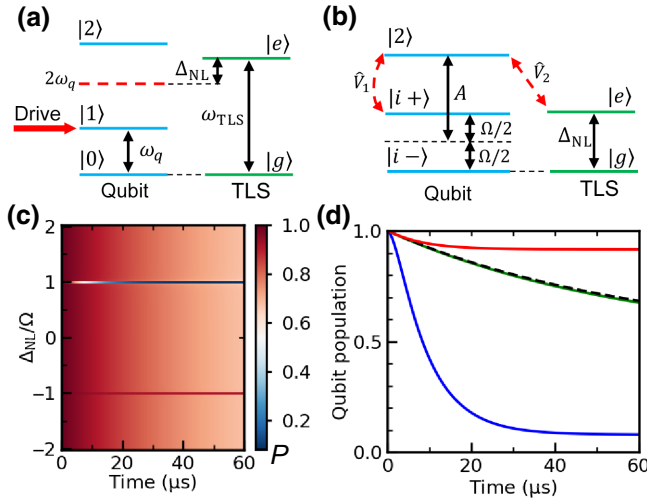


FIG. 2. (a),(b) Schematics of energy levels of a qubit and a critical-current defect in the (a) laboratory frame and (b) rotating frame for $\Delta_{NL} > 0$. Here, \hat{V}_1 and \hat{V}_2 correspond to the interaction terms described in Eqs. (32) and (33), respectively. (c),(d) Results of numerical simulations of the system evolution for a given Rabi frequency in the case of a critical-current-fluctuation TLS defect. (c) Population of the qubit state $|i+\rangle$ as a function of the evolution time and qubit-defect detuning. The qubit is dynamically coupled to the defect when the condition given by Eq. (29) is met. (d) Qubit population at the qubit-defect detunings $\Delta_{NL} = \Omega$ (blue line), $\Delta_{NL} = -\Omega$ (red line), and $\Delta_{NL} \neq \pm\Omega$ (green line). The dashed black line corresponds to the exponential decay $f(t) = [1 + \exp(-\Gamma_{1q}t/2)]/2$.

state $|g\rangle$. The simulation parameters are $\Omega/2\pi = 25$ MHz, $A/2\pi = 1$ GHz, $g_I^{(2)}/2\pi = 2$ MHz, $\Gamma_{1q} = 0.03 \mu\text{s}^{-1}$, and $\Gamma_{1\text{TLS}} = 1 \mu\text{s}^{-1}$. The population of the qubit state $|i+\rangle$ is shown in Figs. 2(c) and 2(d).

The condition for the dynamical coupling between a qubit and a defect with a nonlinear (NL) coupling to the qubit is determined by

$$\Omega = |\Delta_{NL}| = |\omega_{\text{TLS}} - 2\omega_q|, \quad (29)$$

which is different from Eq. (25) for a standard charge-fluctuation defect.

The numerical results imply that the qubit can be coupled to a critical-current defect located close to the double qubit frequency $2\omega_q$, as shown in Fig. 2(a). We further clarify the mechanism of such coupling by rewriting Hamiltonian (27) in the qubit basis $\{|i-\rangle, |i+\rangle, |2\rangle\}$ and defect basis $\{|g\rangle, |e\rangle\}$ in the rotating frame:

$$\hat{H}^R = \hat{H}_0 + \hat{V}_1 + \hat{V}_2. \quad (30)$$

Here the noninteracting term \hat{H}_0 is given by

$$\hat{H}_0 = \frac{\hbar\Omega}{2}(|i+\rangle\langle i+| - |i-\rangle\langle i-|) + \hbar A|2\rangle\langle 2| + \frac{\hbar\Delta_{NL}}{2}\hat{\sigma}_z, \quad (31)$$

and the interaction terms \hat{V}_1 and \hat{V}_2 are given by

$$\hat{V}_1 = \frac{\hbar\Omega}{2}(|i-\rangle\langle 2| - |i+\rangle\langle 2| + \text{H.c.}) \quad (32)$$

and

$$\hat{V}_2 = \hbar g_I^{(2)}(|2, g\rangle\langle i+, e| + |2, g\rangle\langle i-, e| + \text{H.c.}). \quad (33)$$

Using second-order perturbation theory [76], the effective coupling strength between the states $|i+, g\rangle$ and $|i-, e\rangle$ is given by

$$g_{\text{eff}} = \frac{\langle i-, e|\hat{V}_2|2, g\rangle\langle 2, g|\hat{V}_1|i+, g\rangle}{\hbar^2[(\Omega/2) - A]} \approx \frac{g_I^{(2)}\Omega}{2A}, \quad (34)$$

and, thus, the interaction between the qubit and defect is mediated by virtual transitions via the qubit's second excited state, as shown in Fig. 2(b).

An equation similar to condition (29) can be obtained by considering counter-rotating interaction terms omitted in Eq. (27), but the corresponding coupling strength would be smaller than that given by Eq. (34) (details can be found in Appendix D).

III. EXPERIMENTAL DEMONSTRATION

The reported method is experimentally demonstrated by performing TLS defect spectroscopy in a c-shunt flux qubit coupled to a 3D microwave cavity [Figs. 3(a) and 3(b)]. The 3D microwave cavity provided a clean electromagnetic environment without spurious microwave modes, which is important for reliable identification of TLS defects. The qubit is fabricated on a high-resistivity silicon substrate by double-angle shadow evaporation of aluminum. Details of the qubit design can be found in previous work [69]. The qubit is measured via dispersive readout using the experimental setup described in Appendix E. The qubit spectrum as a function of the applied magnetic flux Φ_e is shown in Fig. 3(c). The area of the qubit loop is about $16 \mu\text{m}^2$, and, hence, the magnetic flux bias of $0.5\Phi_0$ corresponds to an applied magnetic field of approximately $65 \mu\text{T}$. By fitting the spectrum using the scQubits PYTHON package [77], the parameters of the c-shunt flux qubit are estimated to be $\alpha \approx 0.457$, $E_C/h \approx 3.2$ GHz, $E_{C_S}/h \approx 0.24$ GHz, and $E_J/h \approx 160$ GHz. In separate measurements at the optimal flux bias point of $\Phi_e = 0.5\Phi_0$, the following system parameters are obtained: cavity resonance frequency $\omega_c/2\pi \approx 8.192$ GHz, qubit transition frequency $\omega_q/2\pi \approx 3.825$ GHz, qubit anharmonicity $A/2\pi \approx 1$ GHz, qubit energy-relaxation time $T_1 \approx 53 \mu\text{s}$, and qubit Hahn-echo dephasing time $T_{2E} \approx 34 \mu\text{s}$.

We detect TLS defects by measuring the qubit excited-state population immediately after the application of a strong microwave drive at the qubit resonance frequency

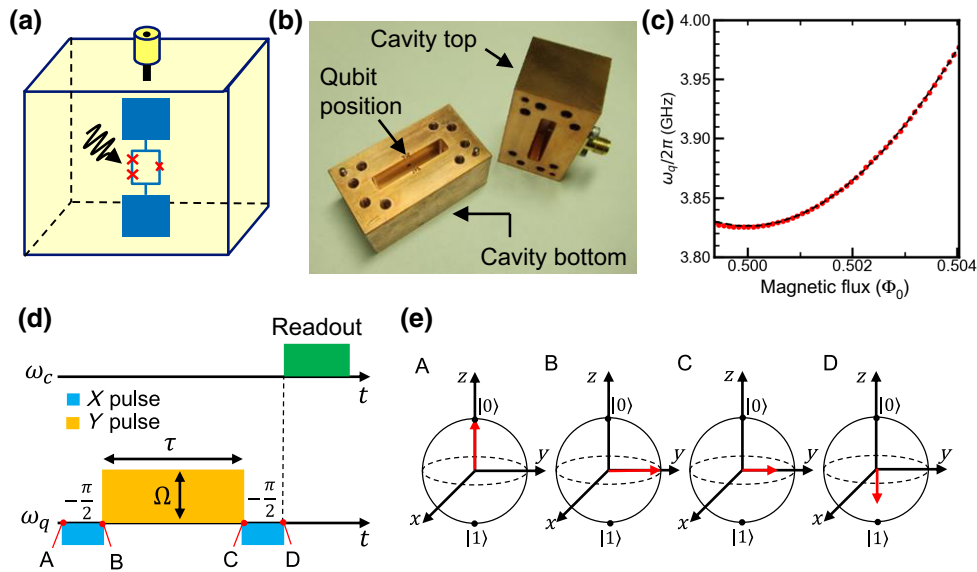


FIG. 3. (a) Schematic of a c-shunt flux qubit embedded inside a 3D microwave cavity. (b) Photograph of the 3D microwave cavity. (c) Qubit spectrum as a function of an applied magnetic flux in units of the magnetic flux quantum Φ_0 . Red dots represent the experimental data. The error bars are within the dot size (the frequency fitting error is less than 0.1 MHz). The dashed black line corresponds to results of numerical simulations using the scQubits package. (d) Schematics of microwave pulse sequences used for the cavity readout (top) and qubit drive (bottom). (e) Bloch-sphere representation of qubit state vectors at different stages of the spin-locking pulse sequence A, B, C, and D shown in Fig. 3(d).

ω_q . The qubit is driven by a so-called spin-locking pulse sequence, where a strong Y pulse of duration τ and amplitude Ω is preceded and followed by low-amplitude X pulses corresponding to $-\pi/2$ rotations of the qubit state vector [Fig. 3(d)]. As shown in Fig. 3(e), the first pulse rotates the qubit state vector around the X axis from the initial $|0\rangle$ state to the $|i+\rangle$ state aligned along the Y axis. The second pulse is a strong microwave Y pulse that rotates the $|i+\rangle$ state around the Y axis and generates the required driving term [Eq. (19)]. The third pulse rotates the qubit state to its final state oriented along the Z axis, and the final qubit population is measured by dispersive readout. Thus, the spin-locking pulse sequence allows us to effectively convert between the qubit states in the basis of $\{|0\rangle, |1\rangle\}$, which is preferable for dispersive readout, and the qubit states in the basis of $\{|i-\rangle, |i+\rangle\}$, which is an eigenstate basis of the strongly driven qubit as described in Sec. II.

Figure 4(a) shows results of the measurement of the qubit excited-state population as a function of the applied magnetic flux and amplitude of the spin-locking Y pulse. Additional time-domain data are shown in Appendix F 3, which correspond to the simulations shown in Figs. 1(c) and 2(c). In experiments, we recalibrated all flux-dependent measurement parameters—including the cavity frequency, qubit frequency, Rabi frequency, and the corresponding duration of an X pulse—at each applied magnetic flux value. The signal-to-noise ratio is improved by using the phase-cycling method (Appendix F 1). The amplitude of the spin-locking Y pulse is calibrated in units

of the Rabi frequency Ω (Appendix F 2). The appropriate duration of the spin-locking Y pulse $\tau = 60 \mu\text{s}$ is determined in time-domain measurements (Appendix F 3). The amplitudes of X pulses are fixed (in voltage units), while their duration is adjusted at each magnetic flux bias to ensure the required rotation angle. Typically, the X-pulse duration is about 40 ns. The repetition period of the sequence is sufficiently long (typically, about 1 ms) to keep the temperature of the mixing chamber stage of the dilution refrigerator below 30 mK.

Pronounced spectral lines TLS1–TLS5 are observed in the experimental data [Figs. 4(b) and 5(a)]. Spectral lines TLS1, TLS2, and TLS3 are fit by Eq. (25) with the TLS defect frequencies $\omega_{\text{TLS1}}/2\pi \approx 3.795$ GHz, $\omega_{\text{TLS2}}/2\pi \approx 3.895$ GHz, and $\omega_{\text{TLS3}}/2\pi \approx 3.915$ GHz. Thus, spectral lines TLS1–TLS3 are due to the interactions between the qubit and conventional charge-fluctuation TLS defects. Since the qubit frequency is greater than the frequency ω_{TLS1} in the whole range of the applied magnetic flux bias, the qubit-defect detuning is negative, $\Delta_L < 0$, and hence, spectral line TLS1 is described by the equation $\Omega = \omega_q - \omega_{\text{TLS1}}$. As for the TLS defects corresponding to spectral lines TLS2 and TLS3, the qubit frequency is less than the frequencies ω_{TLS2} and ω_{TLS3} near the optimal flux bias point, but the qubit transition frequency crosses the defect levels at flux bias values close to $\Phi_e \approx 0.503\Phi_0$. Therefore, spectral lines TLS2 and TLS3 can be fit by equations $\Omega = \omega_{\text{TLS2}} - \omega_q$ and $\Omega = \omega_{\text{TLS3}} - \omega_q$ in the vicinity of the optimal point, and by equations $\Omega =$

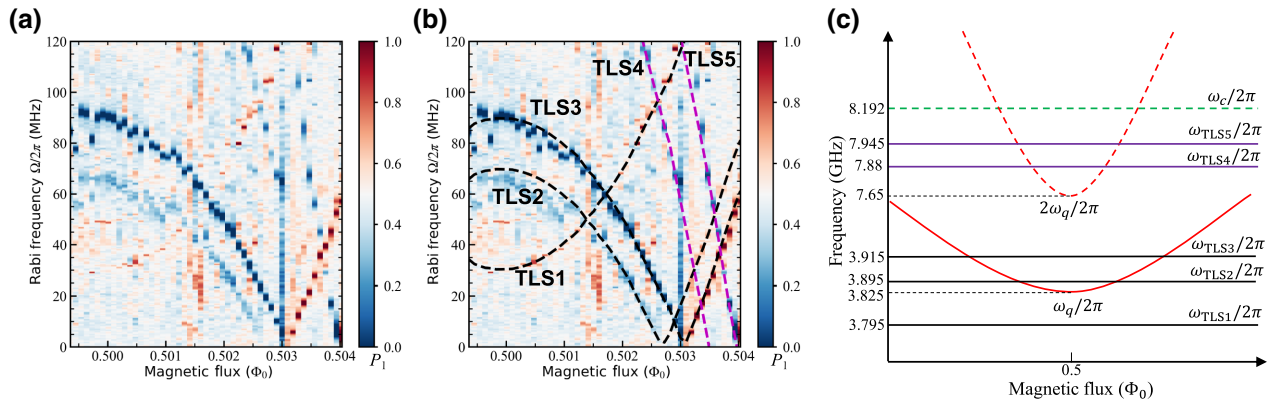


FIG. 4. Experimental demonstration of TLS defect detection using a strong qubit drive. (a) Final excited-state qubit population as a function of the applied magnetic flux and the qubit drive amplitude in Rabi-frequency units. (b) Results of the fitting of the experimental data. Spectral lines TLS1, TLS2, and TLS3 can be fit by Eq. (25) that corresponds to charge-fluctuation TLS defects. Spectral lines TLS4 and TLS5 can be fit by Eq. (29) that corresponds to critical-current-fluctuation TLS defects. (c) Energy level diagram of the system (not to scale). Solid and dashed red lines correspond to the qubit transition frequency ω_q and the double value of ω_q , respectively. Black and magenta horizontal lines represent charge-fluctuation and critical-current-fluctuation TLS defects, respectively. The dashed green line corresponds to the cavity resonance frequency.

$\omega_q - \omega_{\text{TLS2}}$ and $\Omega = \omega_q - \omega_{\text{TLS3}}$ at magnetic flux values $\Phi_e \gtrsim 0.503\Phi_0$, respectively. The interaction between the qubit and TLS defects with positive (negative) values of the defect-qubit detuning, $\Delta_L > 0$ ($\Delta_L < 0$), results in the formation of local minima (maxima) in the qubit population signal. Thus, spectral lines TLS2 and TLS3 have two different “polarities” depending on the applied magnetic flux bias, and they change their “polarity” near the flux bias $\Phi_e = 0.503\Phi_0$, where the corresponding TLS defects have $\Delta_L = 0$. This behavior is consistent with the predictions of the theoretical model described in Sec. II. No avoided crossing is observed in the qubit spectrum near $\Phi_e \approx 0.503\Phi_0$, but the qubit Rabi oscillations are suppressed due to the resonant qubit-defect interaction. Therefore, at that particular magnetic flux value, the automatic procedure of the measurement parameter recalibration does not provide correct values, resulting in the appearance of the vertical line at $\Phi_e \approx 0.503\Phi_0$ in Figs. 4(a) and 4(b). By fitting the time-domain spin-locking data (Appendix F3), we estimate the values of the charge-fluctuation coupling strength $g_C/2\pi \approx 50$ kHz and defect relaxation rate $\Gamma_{\text{TLS}} \approx 1 \mu\text{s}^{-1}$, which are consistent with the values reported in previous work [26,29,56].

In contrast to the spectral features of TLS1–TLS3, the positions of spectral lines TLS4 and TLS5 cannot be described by Eq. (25). Instead, the spectral signatures of TLS4 and TLS5 are fit by Eq. (29) with TLS defect frequencies $\omega_{\text{TLS4}}/2\pi \approx 7.88$ GHz and $\omega_{\text{TLS5}}/2\pi \approx 7.945$ GHz, respectively. Thus, spectral lines TLS4 and TLS5 are formed due to the interaction between the qubit and critical-current-fluctuation defects. By fitting the experimental data obtained in time-domain spin-locking measurements at a fixed magnetic flux bias (Appendix F3),

the typical coupling strength between the qubit and TLS5 defect is estimated to be in the range $g_I^{(2)}/2\pi \approx 8$ –22 MHz, corresponding to an effective coupling strength of up to 1 MHz according to Eq. (34). Using Eq. (16), the relative critical-current fluctuation $r = \delta I_{\text{TLS}}/\alpha I_c$ is calculated to be in the range $r \approx 0.002$ –0.006. Based on the measurements of the $1/f$ critical-current noise in Josephson junctions at low frequencies, the value of the relative critical-current fluctuation due to a single TLS defect is estimated to be $r_0 \approx 10^{-4}$ for an aluminum-oxide junction with an area of $0.08 \mu\text{m}^2$ [18]. In our case, the area of the small junction is about $0.01 \mu\text{m}^2$, and, by scaling the value of r_0 by the ratio of the junction areas, we obtain $r_0 \approx 8 \times 10^{-4}$ for our qubit, which is close to the values r estimated from the experimental data. Here, we assumed that the qubit is coupled to a single TLS defect (if the qubit is coupled to an ensemble of TLS defects, the effective coupling strength will scale with the square root of the total defect number). It should also be noted that the value of r_0 can depend on the junction fabrication technology.

The experimental results shown in Figs. 4(a) and 4(b) can also be plotted as a function of the qubit frequency ω_q and the drive amplitude Ω [Fig. 5(a)]. Here, the conversion between the applied flux bias and qubit frequency is performed using the qubit spectrum data $\omega_q(\Phi_e)$ presented in Fig. 3(c). Experimental results can be reproduced well by numerical simulations of the driven qubit evolution as a function of the qubit frequency [Fig. 5(b)–5(d)]. Here, Fig. 5(b) shows results of calculations using a time-dependent system Hamiltonian without RWA (details can be found in Appendix G1). Using that approach, it is possible to model all types of TLS defects simultaneously, but with the drawback of a long computation

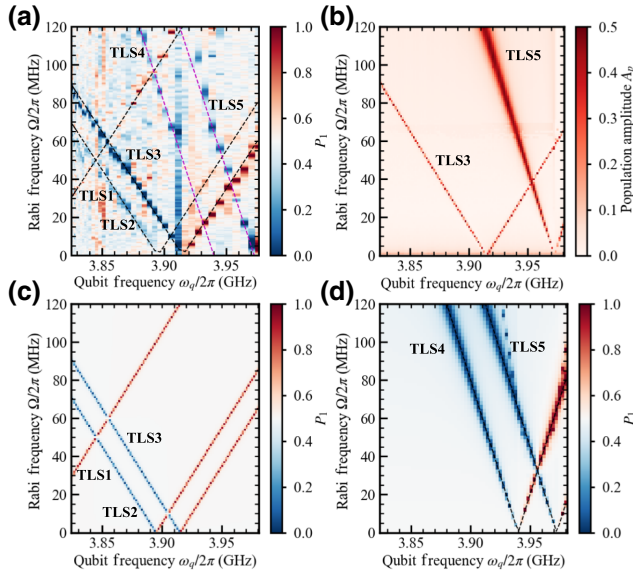


FIG. 5. (a) Experimental data shown in Figs. 4(a) and 4(b) plotted as a function of the qubit frequency ω_q . Straight dashed lines represent analytic equations described in the text. (b) Results of numerical simulations of the system evolution using a time-dependent system Hamiltonian without RWA. The system consists of the qubit, charge defect TLS3, and critical-current defect TLS5 (other defects are not included in the numerical model in order to minimize the calculation time). The amplitude of qubit population oscillations is calculated using the procedure described in Appendix G 1. (c),(d) Results of numerical calculations of the hybrid system evolution using RWA. The system consists of the qubit coupled to (c) charge-fluctuation defects TLS1–TLS3 and (d) critical-current-fluctuation defects TLS4 and TLS5, described by Eqs. (24) and (27), respectively.

time. Simulations can be performed more efficiently using RWA, but, in this case, it is necessary to simulate each type of TLS defect separately, since different types of TLS defect require different RWA transformations (details can be found in Appendix B). For example, Figs. 5(c) and 5(d) show results of separate numerical simulations of charge-fluctuation and critical-current fluctuation TLS defects using Eqs. (24) and (27), respectively. In the numerical calculations, the coupling strengths for charge defects and critical-current defects are $g_C/2\pi \approx 100$ kHz and $g_I^{(2)}/2\pi = 20$ MHz, respectively, and the relaxation rates are the same for all TLS defects, $\Gamma_{\text{TLS}} \approx 1 \mu\text{s}^{-1}$. As shown in Figs. 5(b) and 5(d), spectral lines corresponding to the critical-current-fluctuation defects become less pronounced at small drive amplitudes Ω , which is in qualitative agreement with the analytic prediction given by Eq. (34). We are also able to reproduce different signal “polarities” in Figs. 5(c) and 5(d). Clearly, our theoretical model accounts for the experimental findings.

It was previously shown that detrimental effects of TLS defects can be mitigated by saturating TLS defects using a direct microwave excitation [32,78], or by utilizing a qubit

to heat or cool its TLS environment via a dynamical polarization effect [79]. In our experiments, a strong microwave drive is applied at the qubit transition frequency, and, hence, TLS defects are not excited directly. As for the dynamical polarization method, the qubit-defect interaction rates are much smaller than the energy-relaxation rates of TLS defects, and, therefore, we cannot saturate TLS defects even at high drive amplitudes.

We repeated TLS spectroscopy measurements with an applied in-plane magnetic field of about 0.2 mT (Appendix F 4). We find no dependence of spectral line positions on the applied magnetic field, and, hence, the observed TLS defects are charge defects. We also find that defect frequencies slightly drift on a time scale of days during the same cooldown, and spectral distributions of TLS defects are different for different cooldowns of the same device.

IV. DISCUSSION

Building a realistic noise model of quantum processors is crucial for the progress of NISQ computing [5–7] and performance of quantum error correction protocols with biased-noise superconducting qubits [80–83]. For example, in the models of highly biased noise, it is usually assumed that Z errors (dephasing) occur much more frequently than X and Y errors (energy relaxation). The presence of an off-resonant parasitic TLS defect can increase the rates of X and Y errors, since transverse qubit-defect interaction terms given by Eqs. (12) and (17) provide additional channels for energy relaxation. Therefore, a thorough characterization of off-resonant TLS defects is important for the determination of the dominant type of noise errors for a given qubit drive amplitude. The presented method of TLS defect spectroscopy provides information about the spectral distribution of off-resonant TLS defects, and it allows one to determine the exact form of qubit-defect interaction that is not accessible using other experimental techniques.

The reported technique allows us to consistently distinguish between charge-fluctuation and critical-current-fluctuation TLS defects. Although high-frequency critical-current-fluctuation defects were discussed previously in the relation to experiments with phase qubits [18], it was later shown that those results were better described by charge fluctuations [19]. Regarding the interaction between a qubit and a critical-current-fluctuation defect, the key difference between a phase qubit and the c-shunt flux qubit used in this work is that a phase qubit is typically biased near the critical current of its Josephson junction, where the superconducting phase difference across the Josephson junction φ is close to $\pi/2$ [18]. In that case, the coupling term between a phase qubit and a critical-current TLS defect is linear and proportional to $\cos \varphi \sim \tilde{\varphi}$, where $\tilde{\varphi} = \varphi - \pi/2$. In contrast, in the case of the c-shunt flux qubit biased near the optimal point

$\Phi_e = 0.5\Phi_0$, the effective phase φ is small, $\varphi \approx 0$, and the qubit is coupled to critical-current defects via a nonlinear term proportional to $\cos \varphi \sim \varphi^2$. This nonlinearity allows us to reliably distinguish critical-current TLS defects from standard charge TLS defects with a linear coupling. The reported results demonstrate that critical-current noise is particularly relevant for capacitively shunted qubits, for which the characteristic Josephson energy E_J is large, while the charge noise is suppressed by the large shunt capacitance, $E_J \gg E_{C_S}$. It should be noted that a nonlinear coupling to critical-current defects should be present in other types of qubits, including fixed-frequency transmons [70] and flux-tunable SNAIL transmons [14,84]. The method described in this work can be used for testing new materials and fabrication techniques that aim at minimizing the number of TLS defects in superconducting qubits, such as Josephson-junction fabrication based on epitaxial trilayer structures [15,85].

Our work implies that off-resonant high-frequency TLS defects can significantly affect the dynamics of a superconducting qubit. In the simplest case of a single charge-fluctuation TLS defect, the single-excitation subspace $\{|1g\rangle, |0e\rangle\}$ is coherently mixed due to the always-on transverse qubit-defect coupling, and the eigenstates of the coupled system can be approximated by entangled states [65]

$$\begin{aligned} \overline{|1g\rangle} &= \sqrt{1 - \left(\frac{g}{\Delta}\right)^2} |1g\rangle - \frac{g}{\Delta} |0e\rangle, \\ \overline{|0e\rangle} &= \sqrt{1 - \left(\frac{g}{\Delta}\right)^2} |0e\rangle + \frac{g}{\Delta} |1g\rangle, \end{aligned} \quad (35)$$

where g and $\Delta = \omega_{\text{TLS}} - \omega_q$ are the qubit-defect coupling strength and frequency detuning, respectively, and it is assumed that the system is in the dispersive regime, $g \ll \Delta$. If the measurement process occurs in the qubit bare state basis, the state $\overline{|1g\rangle}$ can be “erroneously” measured as $|0e\rangle$ with a probability of $(g/\Delta)^2$, which results in additional measurement error of the order of $(g/\Delta)^2$ depending on the details of the measurement process [63–65]. On the other hand, if the qubit is initialized in the bare state $|1g\rangle$, the qubit time evolution would be characterized by fast small-amplitude beatings between the eigenmodes, which would affect qubit gate errors [63]. According to our numerical simulations, such types of errors can be mitigated by setting the gate duration to the optimal value $t_g^{\text{opt}} = C_g \times 2\pi/|\Delta|$, where the parameter C_g depends on details of a particular qubit gate implementation and should be determined numerically (Appendix G 2). The significance of the reported method of TLS defect detection is that it allows one to extract detailed information about off-resonant TLS defects in a given qubit that can

be then used for numerical optimization of relevant gate parameters.

According to numerical simulations, similar phenomena of dynamical coupling between a qubit and an off-resonant TLS defect can be observed when the qubit is strongly driven by other pulse sequences, such as a Rabi drive (Appendix G 3).

The described approach for detection of high-frequency TLS defects complements techniques for probing low-frequency TLS defects using a spin-locking pulse sequence [57]. For low-frequency TLS signatures, the condition of resonant qubit-defect interaction is given by the Hartmann-Hahn-type equation $\Omega = \omega_{\text{TLS}}$, and, therefore, in contrast to high-frequency TLS defects, positions of low-frequency TLS signatures will not change significantly in the narrow range of magnetic flux biases used in this work.

V. CONCLUSIONS

We introduced and experimentally demonstrated a method of high-frequency TLS defect spectroscopy in superconducting qubits that allowed us to distinguish between defects with different types of qubit-defect interaction. Using this method, we succeeded in the unambiguous detection of critical-current-fluctuation TLS defects that remained elusive until now. The described technique should also be suitable for detection of other types of high-frequency defects, such as spin defects [86–90]. We envision that the reported method will become a standard protocol for systematic studies of high-frequency defects in both flux-tunable and fixed-frequency superconducting qubits, revealing new insights into the microscopic origin of TLS defects and their mitigation strategies. The presented approach complements methods for the characterization of other types of noise in superconducting qubits, facilitating further improvement in the performance of superconducting quantum processors.

ACKNOWLEDGMENTS

We appreciate William J. Munro for helpful discussions and for granting access to an HPC server for numerical simulations. We thank Aijiro Saito for his technical support with the qubit fabrication. Y.M. acknowledges support from the Leading Initiative for Excellent Young Researchers, MEXT Japan, and JST PRESTO (Grant No. JPMJPR1919), Japan. This work is partially supported by JST CREST (Grant No. JPMJCR1774) and JST Moonshot R&D (Grant No. JPMJMS2067).

APPENDIX A: TLS DEFECT HAMILTONIAN

In the standard tunneling model, a two-level-system defect can occupy one of the two position states $|L\rangle$ and $|R\rangle$ corresponding to the minima of the double-well potential with the tunneling rate Δ_0 and asymmetry energy $\hbar\varepsilon$ [27].

The effective Hamiltonian in the position basis is given by

$$\hat{H}_{\text{TLS}} = \frac{1}{2}\hbar\varepsilon\hat{\sigma}_z^{(p)} + \frac{1}{2}\hbar\Delta_0\hat{\sigma}_x^{(p)}, \quad (\text{A1})$$

where $\hat{\sigma}_z^{(p)} = |R\rangle\langle R| - |L\rangle\langle L|$ and $\hat{\sigma}_x^{(p)} = |R\rangle\langle L| + |L\rangle\langle R|$.

The transformation from the position basis to the eigenstate basis is performed by rotation through angle $\theta = \arctan(\Delta_0/\varepsilon)$,

$$\hat{\sigma}_x^{(p)} = \cos\theta\hat{\sigma}_x + \sin\theta\hat{\sigma}_z, \quad (\text{A2a})$$

$$\hat{\sigma}_y^{(p)} = \hat{\sigma}_y, \quad (\text{A2b})$$

$$\hat{\sigma}_z^{(p)} = \cos\theta\hat{\sigma}_z - \sin\theta\hat{\sigma}_x, \quad (\text{A2c})$$

and the Hamiltonian of the TLS defect in the eigenstate basis is given by

$$\hat{H}_{\text{TLS}} = \frac{1}{2}\hbar\sqrt{\varepsilon^2 + \Delta_0^2}\hat{\sigma}_z = \frac{1}{2}\hbar\omega_{\text{TLS}}\hat{\sigma}_z. \quad (\text{A3})$$

For simplicity, the asymmetry parameter ε is assumed to be negligible throughout this work, $\varepsilon \approx 0$, and, hence, $\theta = \pi/2$. Then the relations between operators in position and eigenstate bases are given by

$$\hat{\sigma}_x^{(p)} = \hat{\sigma}_z, \quad \hat{\sigma}_y^{(p)} = \hat{\sigma}_y, \quad \hat{\sigma}_z^{(p)} = -\hat{\sigma}_x. \quad (\text{A4})$$

APPENDIX B: ROTATING-WAVE APPROXIMATION

The transformation from the laboratory frame Hamiltonian \hat{H} to the rotating frame Hamiltonian \hat{H}^R is determined by

$$\hat{H}^R = \hat{U}\hat{H}\hat{U}^\dagger - \hat{R}, \quad (\text{B1})$$

where the unitary transformation \hat{U} is given by

$$\hat{U} = e^{i\hat{R}t/\hbar}. \quad (\text{B2})$$

In the case of the charge-fluctuation TLS defect, we use the operator

$$\hat{R}_C = \hbar\omega_q\left(\hat{b}^\dagger\hat{b} + \frac{1}{2}\hat{\sigma}_z\right). \quad (\text{B3})$$

It can be shown that the \hat{R}_C operator results in the RWA transformation

$$\begin{aligned} \hat{U}\hat{b}\hat{U}^\dagger &= \hat{b}e^{-i\omega_q t}, \\ \hat{U}\hat{\sigma}_-\hat{U}^\dagger &= \hat{\sigma}_-e^{-i\omega_q t}. \end{aligned} \quad (\text{B4})$$

In the case of the critical-current-fluctuation TLS defect, we use the operator

$$\hat{R}_I = \hbar\omega_q(\hat{b}^\dagger\hat{b} + \hat{\sigma}_z), \quad (\text{B5})$$

and the corresponding RWA transformation is given by

$$\begin{aligned} \hat{U}\hat{b}\hat{U}^\dagger &= \hat{b}e^{-i\omega_q t}, \\ \hat{U}\hat{\sigma}_-\hat{U}^\dagger &= \hat{\sigma}_-e^{-2i\omega_q t}. \end{aligned} \quad (\text{B6})$$

APPENDIX C: POPULATION TRANSFER IN THE CASE OF “HOT” AND “COLD” TLS DEFECTS

Figure 6 illustrates the population transfer mechanism in the rotating frame in the case of a “hot” TLS defect. Here, we consider a charge-fluctuation TLS defect with negative detuning, $\Delta_L < 0$. As described in the main text, it is assumed that there is no dephasing, and the collapse operators for qubit and defect relaxation processes are chosen in the forms $\hat{C}_1 \propto \hat{b}$ and $\hat{C}_2 \propto \hat{\sigma}_-$, respectively. Initially, in the rotating frame, the excited states of the qubit and defect are populated [Fig. 6(a)], and, hence, there is no population transfer between them. Here, the excited state of the TLS defect in the rotating frame $|g\rangle$ corresponds to the defect ground state in the laboratory frame, and, therefore, the TLS defect in state $|g\rangle$ does not relax. After the qubit relaxes from $|i+\rangle$ to a mixed state [Fig. 6(b)], population transfer between the qubit and TLS defect occurs: the qubit and defect are flipped to states $|i+\rangle$ and $|e\rangle$, respectively [Fig. 6(c)]. Finally, the TLS defect relaxes to state $|g\rangle$ [Fig. 6(d)]. The described mechanism explains the high level of population of state $|i+\rangle$ observed in the case of $\Delta_L < 0$. The detailed description of that process would require solving rate equations, which is beyond the scope of this work.

For comparison, Fig. 7 demonstrates the population transfer mechanism in the rotating frame in the case of a “cold” TLS defect ($\Delta_L > 0$).

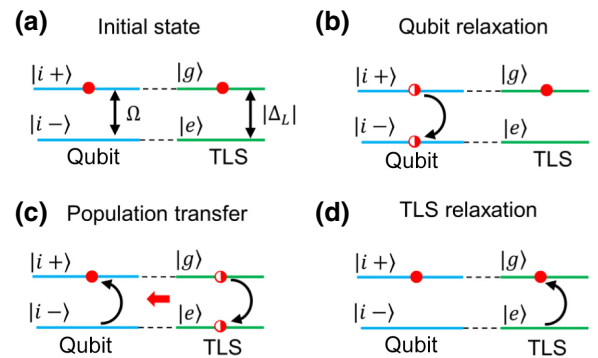


FIG. 6. Population transfer mechanism in the case of a “hot” TLS defect ($\Delta_L < 0$). Energy level diagrams in the rotating frame are shown at different stages of the population transfer process. (a) Qubit and defect are initialized to states $|i+\rangle$ and $|g\rangle$, respectively. (b) Qubit population is distributed between state $|i+\rangle$ and state $|i-\rangle$ due to the qubit relaxation process. (c) Population is transferred from the TLS defect to the qubit. (d) TLS defect is reset to state $|g\rangle$ by the defect energy relaxation process.

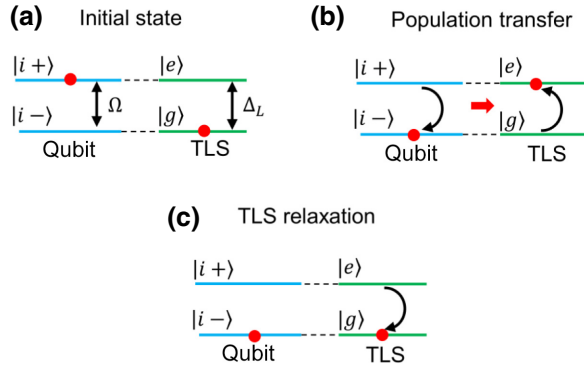


FIG. 7. Population transfer mechanism in the case of a “cold” TLS defect ($\Delta_L > 0$). Energy level diagrams in the rotating frame are shown at different stages of the population transfer process. (a) Qubit and defect are initialized to states $|i+\rangle$ and $|g\rangle$, respectively. (b) Population is transferred from the qubit to the TLS defect. (c) TLS defect is reset to state $|g\rangle$ by the defect energy relaxation process.

APPENDIX D: EFFECT OF COUNTER-ROTATING COUPLINGS

In this section, we consider a different model of the coupling between a qubit and a critical-current defect by taking into account counter-rotating terms omitted in Eq. (27). We start from Hamiltonian (26). The nonlinear interaction term given by Eq. (17) can be expanded in the form

$$\hat{H}_{\text{int}}^{(I)} = \hbar g_I^{(2)} \hat{\sigma}_x ((\hat{b}^\dagger)^2 + \hat{b}^2 + 2\hat{b}^\dagger \hat{b} + 1). \quad (\text{D1})$$

In the main text, the term proportional to $\hat{b}^\dagger \hat{b}$ was eliminated by using the RWA. In this section, we take into account the effect of this interaction beyond the RWA. We consider the interaction Hamiltonian

$$\hat{H}'_{\text{int}} = 2\hbar g_I^{(2)} \hat{\sigma}_x \hat{b}^\dagger \hat{b}. \quad (\text{D2})$$

By truncating the qubit Hilbert space to the lowest two states, we can use the following relations between bosonic operators and qubit Pauli operators $\hat{\tau}_{x,y,z}$ in the eigenstate basis $\{|0\rangle, |1\rangle\}$:

$$\hat{b} = \hat{\tau}_+ = \frac{1}{2}(\hat{\tau}_x + i\hat{\tau}_y), \quad (\text{D3a})$$

$$\hat{b}^\dagger = \hat{\tau}_- = \frac{1}{2}(\hat{\tau}_x - i\hat{\tau}_y), \quad (\text{D3b})$$

$$\hat{b}^\dagger \hat{b} = \frac{1}{2}(1 - \hat{\tau}_z). \quad (\text{D3c})$$

The interaction term between the qubit and a critical-current defect can be written as

$$\hat{H}'_{\text{int}} = -\hbar g_I^{(2)} \hat{\tau}_z \hat{\sigma}_x. \quad (\text{D4})$$

Then, the system Hamiltonian is given by

$$\hat{H} = -\frac{1}{2}\hbar\omega_q \hat{\tau}_z + \frac{1}{2}\hbar\omega_{\text{TLS}} \hat{\sigma}_z - \hbar g_I^{(2)} \hat{\tau}_z \hat{\sigma}_x + \hbar\Omega \cos(\omega_q t) \hat{\tau}_y. \quad (\text{D5})$$

In the rotating frame defined by the rotation operator

$$\hat{R} = -\frac{1}{2}\hbar\omega_q \hat{\tau}_z + \frac{1}{2}\hbar\omega_{\text{TLS}} \hat{\sigma}_z, \quad (\text{D6})$$

the system Hamiltonian is given by

$$\begin{aligned} \hat{H}^{(1)} = & -\hbar g_I^{(2)} \hat{\tau}_z (\hat{\sigma}_+ e^{i\omega_{\text{TLS}} t} + \hat{\sigma}_- e^{-i\omega_{\text{TLS}} t}) + \frac{\hbar\Omega}{2} \hat{\tau}_y \\ & + \frac{i\hbar\Omega}{4} ((\hat{\tau}_x - i\hat{\tau}_y) e^{+2i\omega_q t} - (\hat{\tau}_x + i\hat{\tau}_y) e^{-2i\omega_q t}). \end{aligned} \quad (\text{D7})$$

By changing the qubit basis from the $\hat{\tau}_z$ basis $\{|0\rangle, |1\rangle\}$ to the $\hat{\tau}_y$ basis $\{|i-\rangle, |i+\rangle\}$, we transform the operators $\{\hat{\tau}_x, \hat{\tau}_y, \hat{\tau}_z\}$ to $\{-\hat{s}_y, -\hat{s}_z, \hat{s}_x\}$ and obtain

$$\begin{aligned} \hat{H}^{(1)} = & -\hbar g_I^{(2)} \hat{s}_x (\hat{\sigma}_+ e^{i\omega_{\text{TLS}} t} + \hat{\sigma}_- e^{-i\omega_{\text{TLS}} t}) - \frac{\hbar\Omega}{2} \hat{s}_z \\ & - \frac{i\hbar\Omega}{4} ((\hat{s}_y - i\hat{s}_z) e^{2i\omega_q t} - (\hat{s}_y + i\hat{s}_z) e^{-2i\omega_q t}). \end{aligned} \quad (\text{D8})$$

By going to another rotation frame defined by the operator given by

$$\hat{R}' = -\frac{\hbar\Omega}{2} \hat{s}_z, \quad (\text{D9})$$

we obtain

$$\begin{aligned} \hat{H}' = & -\hbar g_I^{(2)} (\hat{s}_+ e^{-i\Omega t} + \hat{s}_- e^{i\Omega t}) (\hat{\sigma}_+ e^{i\omega_{\text{TLS}} t} + \hat{\sigma}_- e^{-i\omega_{\text{TLS}} t}) \\ & + \frac{\hbar\Omega}{4} ((\hat{s}_- e^{i\Omega t} - \hat{s}_+ e^{-i\Omega t}) e^{2i\omega_q t} - \hat{s}_z e^{2i\omega_q t} + \text{H.c.}). \end{aligned} \quad (\text{D10})$$

After some rearrangement, the Hamiltonian can be written in the form

$$\begin{aligned} \hat{H}'(t) = & -\hbar g_I^{(2)} (\hat{s}_+ \hat{\sigma}_+ e^{i(\omega_{\text{TLS}} - \Omega)t} + \hat{s}_- \hat{\sigma}_- e^{i(\omega_{\text{TLS}} + \Omega)t} + \text{H.c.}) \\ & + \frac{\hbar\Omega}{4} (\hat{s}_- e^{i(2\omega_q + \Omega)t} - \hat{s}_+ e^{i(2\omega_q - \Omega)t} \\ & - \hat{s}_z e^{2i\omega_q t} + \text{H.c.}). \end{aligned} \quad (\text{D11})$$

To simplify the calculation, we assume that

$$\Omega = \omega_{\text{TLS}} - 2\omega_q. \quad (\text{D12})$$

Then, the Hamiltonian can be written as

$$\begin{aligned} \hat{H}'(t) = & -\hbar g_I^{(2)} (\hat{s}_+ \hat{\sigma}_+ e^{2i\omega_q t} + \hat{s}_- \hat{\sigma}_- e^{-2i\omega_q t}) \\ & - \frac{\hbar\Omega}{4} (\hat{s}_z e^{2i\omega_q t} + \hat{s}_z e^{-2i\omega_q t}) + \dots, \end{aligned} \quad (\text{D13})$$

where we have omitted irrelevant terms.

The equation of motion is given by

$$i\hbar \frac{d}{dt} |\psi(t)\rangle = \hat{H}' |\psi(t)\rangle. \quad (\text{D14})$$

By integration from 0 to t , we obtain

$$|\psi(t)\rangle = |\psi(0)\rangle - \frac{i}{\hbar} \int_0^t \hat{H}'(t') |\psi(t')\rangle dt'. \quad (\text{D15})$$

By assuming that H' is small, we use an iteration procedure to write the solution in the form

$$\begin{aligned} |\psi(t)\rangle &= |\psi(0)\rangle - \frac{i}{\hbar} \int_0^t \hat{H}'(t') |\psi(0)\rangle dt' \\ &\quad - \frac{1}{\hbar^2} \int_0^t \hat{H}'(t') dt' \int_0^{t'} \hat{H}'(t'') |\psi(0)\rangle dt''. \end{aligned} \quad (\text{D16})$$

Since \hat{H}' contains only fast oscillating terms, we neglect the second term on the right-hand side of Eq. (D16):

$$\frac{i}{\hbar} \int_0^t \hat{H}'(t') |\psi(0)\rangle dt' \approx 0. \quad (\text{D17})$$

Using Eq. (D13), we write the last term on the right-hand side of Eq. (D16) in the form

$$\begin{aligned} & - \frac{1}{\hbar^2} \int_0^t \hat{H}'(t') dt' \int_0^{t'} \hat{H}'(t'') |\psi(0)\rangle dt'' \\ & \approx - \frac{i}{\hbar} \int_0^t \hat{H}_{\text{eff}} |\psi(0)\rangle dt', \end{aligned} \quad (\text{D18})$$

where we drop fast oscillating terms. Here, the effective Hamiltonian is given by

$$\hat{H}_{\text{eff}} = -\hbar \frac{g_I^{(2)} \Omega}{4\omega_q} (\hat{s}_- \hat{\sigma}_- + \hat{s}_+ \hat{\sigma}_+). \quad (\text{D19})$$

Repeating the same procedure for the condition

$$\Omega = 2\omega_q - \omega_{\text{TLS}}, \quad (\text{D20})$$

we obtain the effective Hamiltonian

$$\hat{H}_{\text{eff}} = \hbar \frac{g_I^{(2)} \Omega}{4\omega_q} (\hat{s}_- \hat{\sigma}_+ + \hat{s}_+ \hat{\sigma}_-). \quad (\text{D21})$$

Thus, if condition (D12) or (D20) is met, there is an effective coupling between the qubit and defect due to counter-rotating terms, but the effective coupling strength is given by

$$g_{\text{eff}} = \frac{g_I^{(2)} \Omega}{4\omega_q}, \quad (\text{D22})$$

which is smaller than the coupling strength value given by Eq. (34).

APPENDIX E: MEASUREMENT SETUP

The measurement setup is similar to that used in Refs. [56,69], with a few modifications made in the measurement circuit (Fig. 8). A broadband 2–18 GHz IQ mixer Marki Microwave MMIQ-0218L is used to generate the qubit drive. A microwave diplexer Marki Microwave DPX-0508 is used to combine the qubit drive and cavity readout signals. The qubit drive is applied via the diplexer low-pass port with the pass band of dc–5 GHz, while the cavity readout is applied through the diplexer high-pass port with the pass band of 8–18 GHz.

APPENDIX F: ADDITIONAL EXPERIMENTAL RESULTS

1. Phase-cycling procedure

Besides the standard spin-locking sequence (sequence 1) described in the main text and shown in Figs. 3(d) and 9(a), we also perform measurements using a modified spin-locking sequence (sequence 2) where the phases of X pulses are inverted [Fig. 9(b)]. In the case of the modified spin-locking pulse sequence, the first X -pulse rotates the qubit state vector around the X axis by an angle $\pi/2$, leaving the qubit in state $|i-\rangle$. We perform numerical simulations of the evolution of the qubit state under a strong Y -pulse drive for the case when the qubit is coupled to a charge-fluctuation defect [Fig. 9(c)]. Except for the initial qubit state, all other simulation parameters are the same as those used in Figs. 1(c) and 1(d). We find that, although the initial states are different, the stationary populations of the $|i+\rangle$ state for sequences 1 and 2 are the same for sufficiently long Y -pulse durations [Fig. 9(d)]:

$$P_+^{(S1)} = P_+^{(S2)} \quad \text{for } t \rightarrow \infty. \quad (\text{F1})$$

However, populations of the final state $|1\rangle$ are different for sequences 1 and 2 (after the X -pulse rotation by $-\pi/2$ and $\pi/2$, respectively):

$$P_1^{(S1)} = P_+^{(S1)} \quad \text{and} \quad P_1^{(S2)} = 1 - P_+^{(S2)}. \quad (\text{F2})$$

Thus, for equal levels of qubit populations in the rotating frame given by Eq. (F1), the final output signals of sequences 1 and 2 have inverted “polarities.”

Because of possible apparatus noise, the actual population values measured in the experiments can have some additional offsets:

$$\begin{aligned} P_1^{(S1)} &= P_+^{(S1)} + N, \\ P_1^{(S2)} &= 1 - P_+^{(S2)} + N, \end{aligned} \quad (\text{F3})$$

with N the offset due to the apparatus noise.

It follows from Eqs. (F1) and (F3) that the apparatus noise can be eliminated by calculating the pure population value

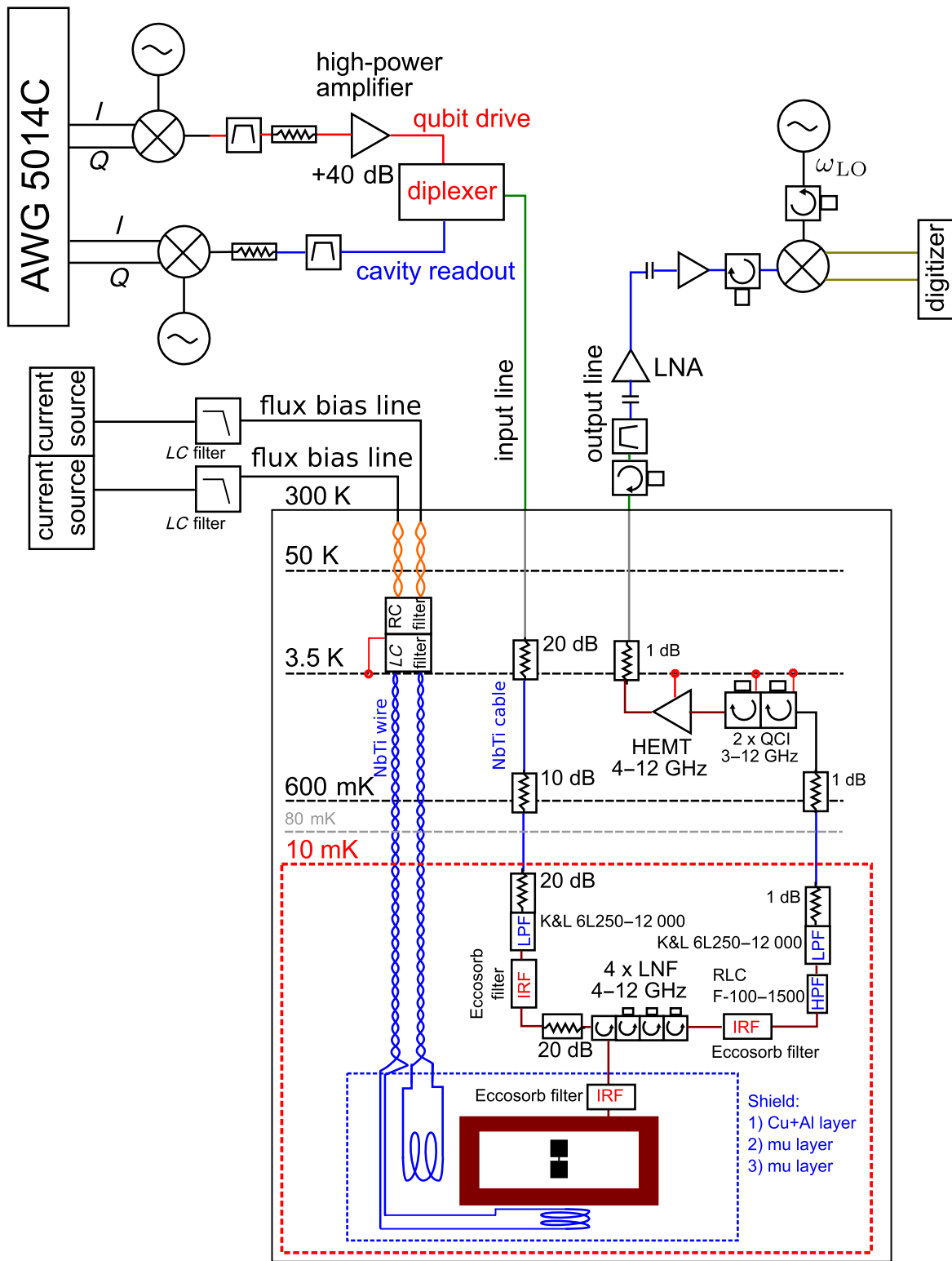


FIG. 8. Schematic of the measurement setup. Here, acronyms AWG, IRF, LPF, LNA stand for an arbitrary waveform generator, an infrared filter, a low-pass filter, and a low-noise amplifier, respectively. QCI corresponds to a QuinStar QCI isolator.

$$P_1 = \frac{1}{2} + \frac{1}{2}(P_1^{(S1)} - P_1^{(S2)}). \quad (F4)$$

The data shown in Figs. 4(a) and 4(b) are processed using the described procedure.

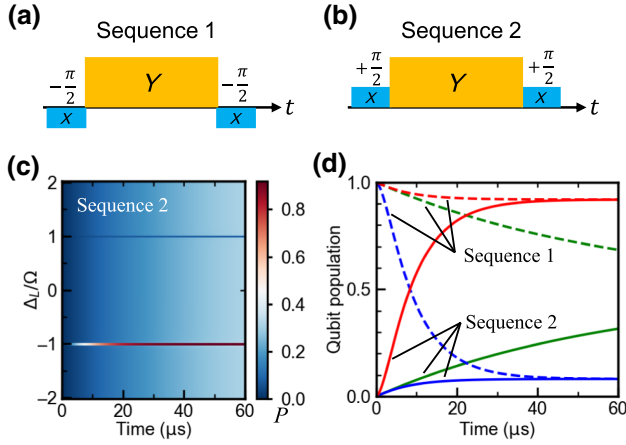


FIG. 9. (a) Schematic of the standard spin-locking sequence used in measurements reported in the main text (sequence 1). (b) Schematic of the modified spin-locking sequence (sequence 2). (c) Results of numerical simulations of the system evolution when the qubit is driven by sequence 2. The population of the qubit state $|i+\rangle$ is shown. The initial qubit state is $|i-\rangle$. The other parameters are the same as those used in Figs. 1(c) and 1(d). (d) Comparison of the qubit response at qubit-defect detunings $\Delta_L = \Omega$ (blue lines), $\Delta_L = -\Omega$ (red lines), and $\Delta_L \neq \pm\Omega$ (green lines). Solid lines correspond to sequence 2 and dashed lines correspond to sequence 1.

2. Rabi frequency calibration

The Rabi frequency Ω is calibrated in separate experiments by measuring the period of Rabi oscillations of the qubit. Dependencies of the Rabi frequency on the drive amplitude and applied magnetic flux are shown in Figs. 10(a) and 10(b), respectively. The slight deviation of the Rabi frequency from a linear fit at high drive amplitudes is due to the low fitting accuracy that is caused by the low sampling rate of the data.

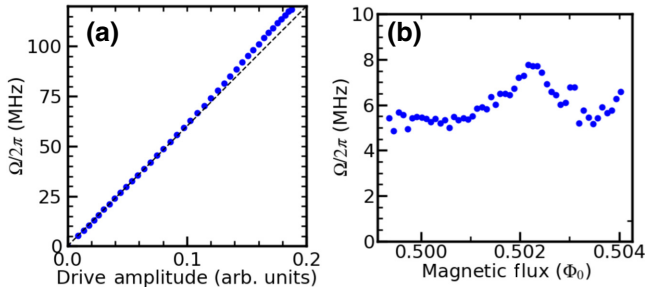


FIG. 10. (a) Dependence of the Rabi frequency on the qubit drive amplitude at the optimal point $\Phi \approx 0.5\Phi_0$. The black dashed line corresponds to a linear function plot, added to guide the eye. (b) Dependence of the Rabi frequency on the applied magnetic flux for a fixed qubit drive amplitude.

3. Time-domain spin-locking measurements

Time-domain spin-locking measurements are performed using the modified spin-locking sequence (sequence 2) described in Appendix F 1. Typical results are shown in Fig. 11. Pronounced horizontal spectral lines are observed at Rabi frequencies where the qubit is dynamically coupled to TLS defects. The Y -pulse duration $60 \mu\text{s}$ is enough to reach the stationary levels of the qubit population.

The parameters of the qubit-defect coupled system can be estimated by fitting the experimental data using the theoretical models described in the main text. Figure 12 shows results of the fitting of time-domain spin-locking data corresponding to a critical-current-fluctuation TLS defect. The qubit-defect coupling strength $g_I^{(2)}$ and defect relaxation rate Γ_{TLS} are used as fitting parameters, and the fitting is performed using the following procedure.

First, by comparing the positions of spectral line TLS5 in Fig. 4(b) and the spectral lines in Fig. 11(b) at the flux bias $0.5039\Phi_0$, we identify that the pronounced spectral line, which is observed in Fig. 11(b) at $\Omega/2\pi \approx 23.4 \text{ MHz}$, corresponds to the critical-current-fluctuation TLS defect [it should be noted that Figs. 4(a) and 4(b) were obtained using the standard spin-locking sequence, while Fig. 11 is obtained using the modified spin-locking sequence, and, hence, the “polarities” of spin-locking signals are inverted]. Thus, at the given flux bias, the qubit-defect detuning is $\Delta_{\text{NL}}/2\pi \approx 23.4 \text{ MHz}$.

Second, we extract two data sets from the data shown in Fig. 11(b): the spin-locking signal at $\Omega/2\pi \approx 23.4 \text{ MHz}$ and another one at $\Omega/2\pi \approx 22.2 \text{ MHz}$ that correspond to effective qubit-defect detunings $\delta\Omega/2\pi = 0 \text{ MHz}$ and $\delta\Omega/2\pi = 1.2 \text{ MHz}$, respectively [Fig. 12(a)]. Here, the effective qubit-defect detuning in the rotating frame is defined as $\delta\Omega = \Delta_{\text{NL}} - \Omega$.

Third, we calculate the root-mean-square (RMS) fitting deviation (fitting residual) σ for each data set using the expression

$$\sigma = \sqrt{\langle [Y_{\text{exp}} - Y_{\text{fit}}(g_I^{(2)}, \Gamma_{\text{TLS}})]^2 \rangle}, \quad (\text{F5})$$

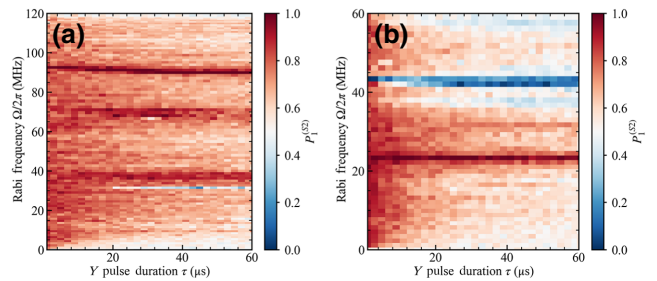


FIG. 11. Typical results of spin-locking measurements using the modified pulse-sequence (sequence 2) at the (a) optimal flux bias point $0.5\Phi_0$ and (b) flux bias $0.5039\Phi_0$. The qubit is initialized in the $|i-\rangle$ state in the rotating frame.

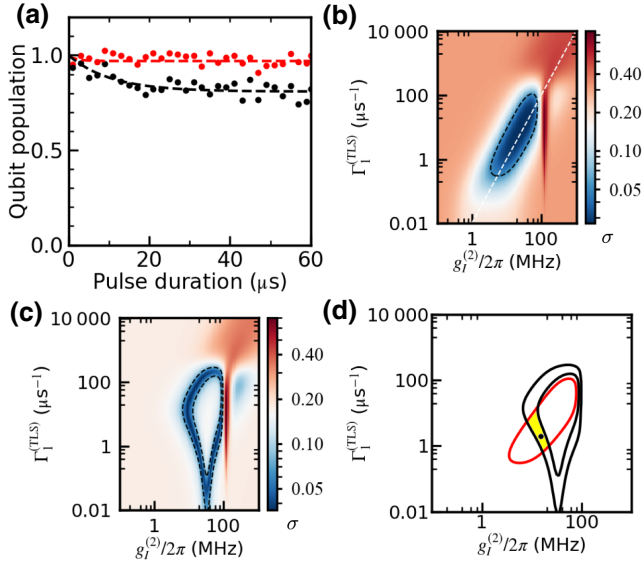


FIG. 12. Results of the fitting of time-domain spin-locking signals corresponding to a critical-current-fluctuation TLS defect. The experimental data points are extracted from the results shown in Fig. 11(b). The qubit is initialized in the $|i-\rangle$ state in the rotating frame. The magnetic flux bias is $0.5039\Phi_0$. At the given bias, the detuning between the qubit and critical-current-fluctuation TLS defect is $\Delta_{\text{NL}}/2\pi \approx 23.4$ MHz. (a) Qubit population decay at Rabi frequencies $\Omega/2\pi \approx 23.4$ MHz (red dots) and $\Omega/2\pi \approx 22.2$ MHz (black dots) where the effective qubit-defect detuning is $\delta\Omega/2\pi = 0$ MHz and $\delta\Omega/2\pi = 1.2$ MHz, respectively. Dashed lines represent results of numerical simulations described in the text. (b) RMS fitting deviation (residual) σ as a function of the fitting parameters $g_I^{(2)}$ and Γ_{ITLS} for the experimental data obtained at $\delta\Omega/2\pi = 0$ MHz. The dashed white line corresponds to the scaling law $\mathcal{F} \propto (g_I^{(2)})^2/\Gamma_{\text{ITLS}}$ (added as a visual guide). The dashed black curve bounds the region of optimal fitting parameters. (c) RMS fitting deviation σ for the experimental data obtained at $\delta\Omega/2\pi = 1.2$ MHz. The dashed black curves bound the regions of optimal fitting parameters. (d) Regions of optimal fitting parameters for $\delta\Omega/2\pi = 0$ MHz (red curve) and $\delta\Omega/2\pi = 1.2$ MHz (black curve). The yellow area corresponds to the overlap between the regions. The black dot corresponds to the fitting values $g_I^{(2)}$ and Γ_{ITLS} used to plot the fitting curves shown in (a).

where Y_{exp} corresponds to a given data set shown in Fig. 12(a), and Y_{fit} is the result of numerical simulations for given fitting parameters $g_I^{(2)}$ and Γ_{ITLS} [Figs. 12(b) and 12(c)]. To calculate Y_{fit} , we numerically solve the master equation for Hamiltonian (27) using the following parameters: $\Delta_{\text{NL}}/2\pi = 23.4$ MHz, $A/2\pi = 1$ GHz, $\Gamma_{1q} = 1/T_1 \approx 0.02 \mu\text{s}^{-1}$, and $\Gamma_{2q} = 1/T_{2E} \approx 0.03 \mu\text{s}^{-1}$. The qubit states are truncated to the lowest three levels. The collapse operators are $\hat{C}_1 = \sqrt{\Gamma_{1q}}\hat{b}$, $\hat{C}_2 = \sqrt{2\Gamma_{2q}}\hat{b}^\dagger\hat{b}$, and $\hat{C}_3 = \sqrt{\Gamma_{\text{ITLS}}}\hat{\sigma}_-$. Here, we phenomenologically introduce the pure dephasing term \hat{C}_2 to improve the fitting accuracy

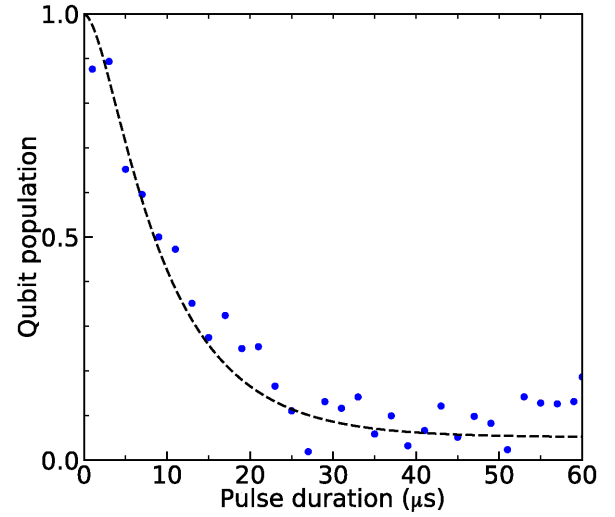


FIG. 13. Results of the fitting of the time-domain spin-locking signal corresponding to a charge-fluctuation TLS defect. The experimental data points are extracted from the results shown in Fig. 11(b). The qubit is initialized in the $|i-\rangle$ state in the rotating frame. The magnetic flux bias is $0.5039\Phi_0$.

for the data at $\delta\Omega/2\pi = 1.2$ MHz. The shape of the pure dephasing term is chosen to be similar to the term typically used for a two-level qubit: $\hat{C}_2 = \sqrt{\Gamma_{2q}/2}\hat{\tau}_z \approx \sqrt{2\Gamma_{2q}}\hat{b}^\dagger\hat{b}$. The qubit is initialized in its ground state $|i-\rangle$ in the rotating frame, the defect is initialized in its ground state $|g\rangle$, and the population of the qubit state $|i-\rangle$ is calculated. Figures 12(b) and 12(c) show fitting deviations for the data obtained at $\delta\Omega/2\pi = 0$ MHz and $\delta\Omega/2\pi = 1.2$ MHz, respectively. The regions of optimal fitting parameters are determined by plotting contour plots at the level of $2\sigma_{\text{min}}$, where σ_{min} is the minimum value of the fitting deviation for a given data set. In the case of $\delta\Omega/2\pi = 0$ MHz, the minimum fitting residual is achieved in the range of fitting parameters that follow the scaling law $\mathcal{F} \propto (g_I^{(2)})^2/\Gamma_{\text{ITLS}}$. This scaling is due to the fact that the qubit-defect system is in the Purcell regime with effective qubit relaxation rate given by $\Gamma_P = 4g_{\text{eff}}^2/\Gamma_{\text{ITLS}}$.

Finally, the region of “global” fitting parameters is determined by finding the overlap of the regions of “local” optimal fitting parameters for $\delta\Omega/2\pi = 0$ MHz and $\delta\Omega/2\pi = 1.2$ MHz [Fig. 12(d)]. Then, the fitting curves shown in Fig. 12(a) are calculated using the fitting parameters from that region: $g_I^{(2)}/2\pi = 15$ MHz and $\Gamma_{\text{ITLS}} = 2 \mu\text{s}^{-1}$.

A similar approach is used to extract characteristics of charge-fluctuation TLS defects. By fitting the time-domain spin-locking data (Fig. 13), the coupling strength and the relaxation rate for charge-fluctuation TLS defects are estimated to be $g_C/2\pi \approx 50$ kHz and $\Gamma_{\text{ITLS}} \approx 1 \mu\text{s}^{-1}$, respectively.

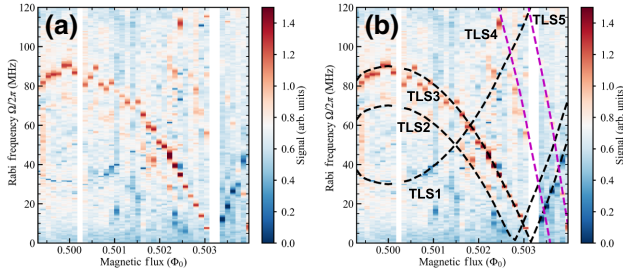


FIG. 14. Results of TLS defect spectroscopy in experiments with an applied in-plane magnetic field of 0.2 mT. The qubit is initialized in the $|i-\rangle$ state in the rotating frame. (a) Excited-state qubit population as a function of the applied magnetic flux and the qubit drive amplitude in units of the Rabi frequency. (b) Comparison of the experimental data obtained at 0.2 mT with the positions of spectral lines TLS1–TLS5 determined in the experiments at 0 mT. Dashed lines are plotted using the same equations and parameters as the dashed lines shown in Fig. 4(b).

4. Dependence on the applied in-plane magnetic field

Figure 14 shows results of TLS defect spectroscopy in experiments with an external magnetic field applied parallel to the qubit surface. The strength of the magnetic field is about 0.2 mT. Experiments are performed using the modified pulse sequence described in Appendix F 1. The positions of spectral signatures of TLS defects are roughly the same in experiments with (Fig. 14) and without (Fig. 4) the in-plane magnetic field.

APPENDIX G: ADDITIONAL NUMERICAL RESULTS

1. Numerical simulations of the system evolution without using RWA

As described in the main text, charge-fluctuation and critical-current-fluctuation TLS defects can be modeled separately using RWAs with two different rotation operators given by Eqs. (B3) and (B5), respectively. However, it is not possible to model defects with different types of qubit-defect interactions simultaneously in the same rotating frame. In order to numerically reproduce the experimental results that include spectral lines of both charge and critical-current TLS defects, we solve a Lindblad master equation for the following time-dependent Hamiltonian without using RWA:

$$\begin{aligned} \frac{\hat{H}_t}{\hbar} = & \left(\omega_q(\Phi_e) - \frac{A}{2} \right) \hat{b}^\dagger \hat{b} + \frac{A}{2} (\hat{b}^\dagger \hat{b})^2 + \frac{\omega_{\text{TLS3}}}{2} \hat{\sigma}_z^{(3)} \\ & + \frac{\omega_{\text{TLS5}}}{2} \hat{\sigma}_z^{(5)} + ig_C \hat{\sigma}_x^{(3)} (\hat{b}^\dagger - \hat{b}) + g_I \hat{\sigma}_x^{(5)} (\hat{b}^\dagger + \hat{b})^2 \\ & + i\Omega \cos(\omega_q t) (\hat{b}^\dagger - \hat{b}). \end{aligned} \quad (\text{G1})$$

Here, the model system consisted of the qubit, charge defect TLS3, and critical-current defect TLS5 (other

defects are not included in the numerical model in order to minimize the calculation time). We also take into account the dependence of the qubit frequency on the applied flux bias Φ_e . It should be noted that a complete derivation of a flux-dependent qubit Hamiltonian in terms of bosonic operators is beyond the scope of this paper, and the first line of Hamiltonian (G1) represents a phenomenological model of a Duffing oscillator with a flux-dependent resonant frequency. The dependence of the qubit frequency on the applied flux bias is shown in Fig. 3(c) in the main text. At each value of the qubit frequency ω_q , the system evolution is calculated for two initial qubit states $|i+\rangle$ and $|i-\rangle$, using the following parameters: $\omega_{\text{TLS3}}/2\pi \approx 3.915$ GHz, $\omega_{\text{TLS5}}/2\pi \approx 7.945$ GHz, $A/2\pi = 1$ GHz, $\Gamma_{1q} = 1/T_1 \approx 0.02 \mu\text{s}^{-1}$, $\Gamma_{\text{TLS3}} = \Gamma_{\text{TLS5}} = 1 \mu\text{s}^{-1}$, $g_C/2\pi = 100$ kHz, and $g_I/2\pi = 20$ MHz. For initial states $|i+\rangle$ and $|i-\rangle$, the population of the qubit state $|i+\rangle$ is calculated as a function of the Rabi frequency and evolution time, $P_+^{(S1)}(\omega_q, \Omega, t)$ and $P_+^{(S2)}(\omega_q, \Omega, t)$, respectively. Figures 15(a) and 15(b) show $P_+^{(S1)}(\omega_q, \Omega, t)$ and $P_+^{(S2)}(\omega_q, \Omega, t)$, respectively, obtained at a given qubit frequency. Since simulations are performed in the laboratory frame, the qubit population signal oscillates with frequency $\omega_q/2\pi$, and it is difficult to distinguish TLS spectral lines in 2D plots. However, the effect of the qubit-TLS interaction on the driven qubit population is clearly observed in individual traces [Fig. 15(c)]. In order to remove the unwanted background, the modified qubit population signal is calculated using the equation

$$P_m(\omega_q, \Omega, t) = \frac{P_+^{(S1)}(\omega_q, \Omega, t) + P_+^{(S2)}(\omega_q, \Omega, t)}{2}. \quad (\text{G2})$$

When there is no interaction between the qubit and a TLS defect, signals $P_+^{(S1)}(\omega_q, \Omega, t)$ and $P_+^{(S2)}(\omega_q, \Omega, t)$ have opposite phases, $P_+^{(S1)}(\omega_q, \Omega, t) = 1 - P_+^{(S2)}(\omega_q, \Omega, t)$, and the modified qubit population signal is constant, $P_m(\omega_q, \Omega, t) = 0.5$. Figure 15(d) shows $P_m(\omega_q, \Omega, t)$ at a given qubit frequency, where we can clearly see a spectral line due to the qubit-defect interaction at Rabi frequency $\Omega/2\pi = 90$ MHz.

The data shown in Fig. 5(b) in the main text represents amplitudes of the modified qubit population oscillations at the end of each simulation that were estimated using the equation

$$A_p = \frac{P_{\min} + P_{\max}}{2}, \quad (\text{G3})$$

where $P_{\min}(\omega_q, \Omega)$ and $P_{\max}(\omega_q, \Omega)$ are the minimum and maximum values of the signal oscillations at the end of a simulation, respectively:

$$P_{\min}(\omega_q, \Omega) = \min_{t_1 - 2T \leq t \leq t_1} P_m(\omega_q, \Omega, t) \quad (\text{G4})$$

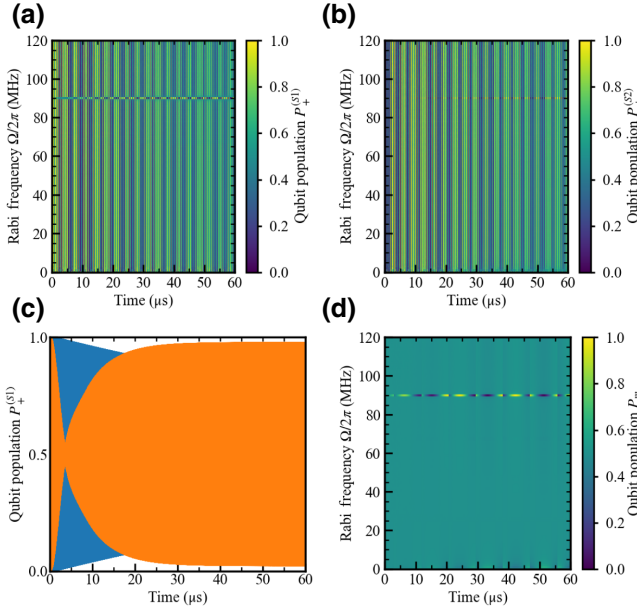


FIG. 15. Time-domain results of numerical simulations of the time-dependent system Hamiltonian without using RWA. The qubit frequency is set to $\omega_q/2\pi \approx 3.825$ GHz. Because of signal fast oscillations, (a), (b), and (d) include plotting artifacts in the form of low-frequency modulations. (a) Simulation results for the initial state $|i+\rangle$. The vertical stripe structure is a plotting artifact (the actual oscillation period is much shorter). (b) Simulation results for the initial state $|i-\rangle$. (c) Traces extracted from the data shown in (a) at Rabi frequencies $\Omega/2\pi = 0$ MHz (blue line) and $\Omega/2\pi = 90$ MHz (orange line). At $\Omega/2\pi = 90$ MHz, the driven qubit evolution is affected by the interaction between the qubit and TLS defect. (d) Arithmetic mean of the data shown in (a) and (b).

and

$$P_{\max}(\omega_q, \Omega) = \max_{t_1 - 2T \leq t \leq t_1} P_m(\omega_q, \Omega, t). \quad (\text{G5})$$

Here, t_1 is the simulation end time and T is the oscillation period.

2. Gate errors due to the interaction between a qubit and an off-resonant TLS defect

In this section, we describe numerical simulations of single-qubit gate errors for the system consisting of the qubit coupled to an off-resonant TLS defect. For simplicity, it is assumed that the defect is a charge-fluctuation TLS defect. We calculate the minimum gate error p as a function of the gate duration t_g and qubit-defect detuning Δ using the procedure described below. We assume here that the value of the qubit-defect coupling strength is $g/2\pi = 500$ kHz, which is larger than that observed in this work, but it is still within the range of defect coupling strengths 5 kHz–50 MHz reported in the literature [19,26,29,56].

The model system Hamiltonian is given in the rotating frame by

$$\hat{H}_S = \hat{H}_0 + \hat{H}_d(t), \quad (\text{G6})$$

where the time-independent term is described by

$$\hat{H}_0 = \frac{1}{2}\hbar\Delta\hat{\sigma}_z + i\hbar g(\hat{\tau}_-\hat{\sigma}_- - \hat{\tau}_+\hat{\sigma}_+) \quad (\text{G7})$$

and the time-dependent drive term is given by

$$\hat{H}_d(t) = \frac{1}{2}\hbar\Omega(t)\hat{O}. \quad (\text{G8})$$

Here, $\hat{\sigma}_z, \hat{\sigma}_\pm = (\hat{\sigma}_x \pm \hat{\sigma}_y)/2$ are Pauli operators of the TLS defect, and $\hat{\tau}_\pm = (\hat{\tau}_x \pm \hat{\tau}_y)/2$ are qubit Pauli operators in the $\{|0\rangle, |1\rangle\}$ basis. Operator \hat{O} determines a particular gate type, and, in this work, two types of gate are simulated: the idle gate ($\hat{O} = \hat{I}$) and the \hat{Y} gate ($\hat{O} = \hat{\tau}_y$). Variable $\Omega(t)$ describes the shape of the drive pulse, and, for simplicity, we assume that the pulse has a Gaussian shape described by the pulse duration t_g , time offset t_{off} , drive amplitude Ω_{\max} , and standard deviation $\sigma_G = t_g/16$:

$$\Omega(t) = \Omega_{\max} e^{-[(t-t_{\text{off}})^2/2\sigma_G^2]}, \quad 0 \leq t \leq t_g. \quad (\text{G9})$$

We calculate the gate error p using the equation

$$p = 1 - F(\rho(t_g), \rho_{\text{target}}), \quad (\text{G10})$$

where $F(\rho(t_g), \rho_{\text{target}})$ is the quantum state fidelities of the forward propagated state and target state described by reduced density matrices of qubit subsystems $\rho(t_g)$ and ρ_{target} , respectively. The density matrix of the forward propagated state is calculated by numerically solving a Lindblad master equation for the system Hamiltonian \hat{H}_S for given values of the pulse duration t_g , time offset t_{off} , drive amplitude Ω_{\max} , and qubit-defect detuning Δ . The initial system state is $|\psi_0\rangle = |1g\rangle$, and the target state is $|\psi_{\text{target}}\rangle = \hat{O}|\psi_0\rangle$. In reported simulations, we used the qubit energy-relaxation and dephasing rates $\Gamma_{1q} = 0.01 \mu\text{s}^{-1}$ and $\Gamma_{2q} = 0.01 \mu\text{s}^{-1}$, respectively, and TLS defect energy-relaxation and dephasing rates $\Gamma_{1\text{TLS}} = 1 \mu\text{s}^{-1}$ and $\Gamma_{2\text{TLS}} = 1 \mu\text{s}^{-1}$, respectively.

For given values of t_g , t_{off} , and Δ , we minimize the gate error p by varying the drive amplitude Ω_{\max} using the Nelder-Mead optimization method in PYTHON. The initial value of Ω_{\max} is equal to $\sqrt{\pi/2}/\sigma_G$, which corresponds to the π rotation of a bare qubit state [as can be shown by integrating Eq. (G9)].

Results of the numerical optimization are shown in Fig. 16. In the case of the idle gate \hat{I} and $g = 0$, the gate error increases with increasing gate duration due to the bare qubit relaxation [Fig. 16(a)]. In the case of the idle gate \hat{I} and $g = 500$ kHz, one can see an oscillation pattern with the characteristic period $2\pi/\Delta$ [Fig. 16(b)]. This

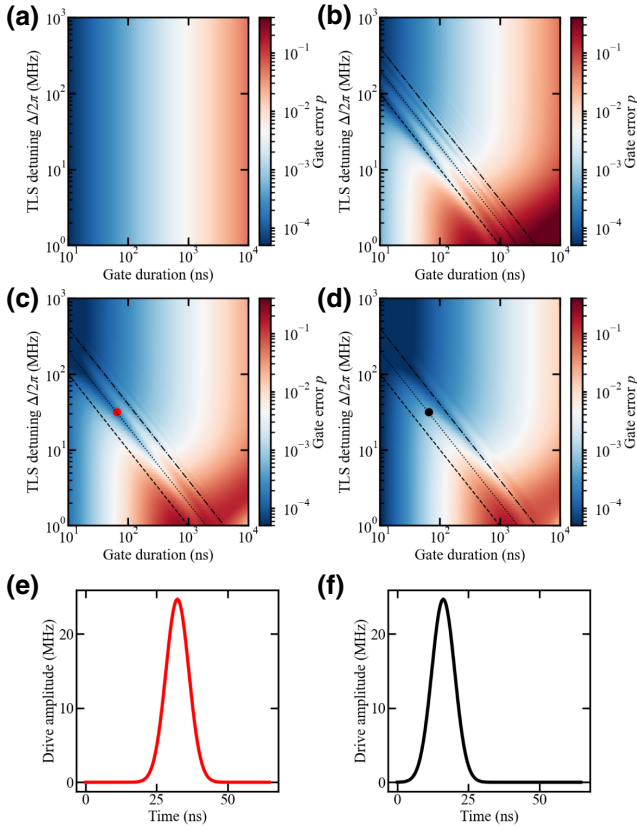


FIG. 16. Results of numerical simulations of single-qubit gate errors as a function of the gate duration t_g and frequency detuning between the qubit and charge-fluctuation TLS defect Δ . (a),(b) Error of the idle gate \hat{I} for qubit-defect coupling strengths (a) $g = 0$ and (b) $g/2\pi = 500$ kHz. (c),(d) Error of the \hat{Y} gate for time offsets (c) $t_{\text{off}} = 0.5t_g$ and (d) $t_{\text{off}} = 0.25t_g$ (in both cases, $g/2\pi = 500$ kHz). The red and black dots in (c) and (d) represent the same values $t_g \approx 65$ ns and $\Delta/2\pi \approx 32$ MHz, and corresponding optimized pulse shapes for given time offsets $t_{\text{off}} = 0.5t_g$ and $t_{\text{off}} = 0.25t_g$ are plotted in (e) and (f), respectively. The dashed, dotted, and dash-dot lines in (b)–(d) correspond to functions $\Delta = C_g \times 2\pi/t_g$ with $C_g = 1, 2,$ and 4 , respectively.

oscillation stems from the always-on nonresonant (dispersive) qubit-defect interaction described in the main text. In addition, the increase in gate error with decreasing qubit-defect detuning due to the Purcell effect is observed. In Figs. 16(c) and 16(d), we plot results of the optimization of \hat{Y} gates implemented using microwave pulses with two different pulse time offsets $t_{\text{off}} = 0.5t_g$ and $t_{\text{off}} = 0.25t_g$, respectively. Examples of optimized pulse shapes at $t_g \approx 65$ ns and $\Delta/2\pi \approx 32$ MHz for given time offsets are shown in Figs. 16(e) and 16(f), respectively. The reason for simulating \hat{Y} gates with different t_{off} is to show that the oscillation patterns are different for different time offsets due to the interplay between the drive-induced rotation of the qubit state vector and its fast small-amplitude precession caused by the dispersive qubit-defect coupling. For a

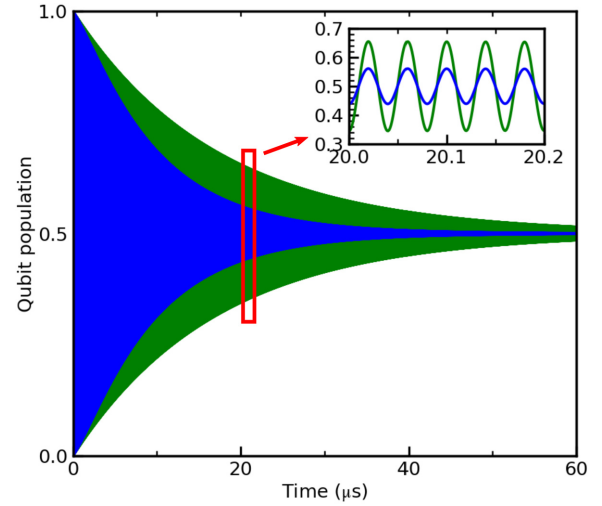


FIG. 17. Results of numerical simulations of the qubit evolution under a strong Rabi drive. The population of the qubit state $|0\rangle$ is shown as a function of the Rabi pulse duration. The blue line represents the Rabi decay of a qubit coupled to an off-resonant TLS defect when the pulse amplitude (Rabi frequency) is equal to the qubit-defect detuning ($\Delta_L = \Omega$). The green curve corresponds to the Rabi decay of a bare qubit ($\Delta_L \neq \pm\Omega$). Inset: an enlarged view showing Rabi oscillations in the range of pulse duration values close to 20 μs .

given qubit-defect detuning Δ , the gate error can be minimized by setting the gate duration to the value $t_g^{\text{opt}} = C_g \times 2\pi/\Delta$, where parameter C_g depends on details of a particular qubit gate implementation and should be determined numerically. For example, $C_g \approx 1$, $C_g \approx 2$, and $C_g \approx 4$ for the gate error simulations shown in Figs. 16(b)–16(d), respectively.

3. Qubit-defect coupling in the case of a Rabi drive

Figure 17 shows results of numerical simulations of the qubit evolution under a strong Rabi drive. Here, the qubit is initialized in state $|0\rangle = (|i-\rangle + |i+\rangle)/\sqrt{2}$. Other parameters are the same as used in the simulations presented in Figs. 1(c) and 1(d). The decay of Rabi oscillations is affected by the interaction between the qubit and off-resonant TLS defect when the Rabi frequency is equal to the absolute value of the qubit-defect detuning.

- [1] M. Kjaergaard, M. E. Schwartz, J. Braumüller, P. Krantz, J. I.-J. Wang, S. Gustavsson, and W. D. Oliver, Superconducting qubits: Current state of play, *Annu. Rev. Condens. Matter Phys.* **11**, 369 (2020).
- [2] A. G. Fowler, M. Mariantoni, J. M. Martinis, and A. N. Cleland, Surface codes: Towards practical large-scale quantum computation, *Phys. Rev. A* **86**, 032324 (2012).

- [3] C. Gidney and M. Ekerå, How to factor 2048 bit RSA integers in 8 hours using 20 million noisy qubits, *Quantum* **5**, 433 (2021).
- [4] E. Gouzien and N. Sangouard, Factoring 2048-Bit RSA Integers in 177 Days with 13 436 Qubits and a Multimode Memory, *Phys. Rev. Lett.* **127**, 140503 (2021).
- [5] J. Preskill, Quantum Computing in the NISQ era and beyond, *Quantum* **2**, 79 (2018).
- [6] K. Bharti, A. Cervera-Lierta, T. H. Kyaw, T. Haug, S. Alperin-Lea, A. Anand, M. Degroote, H. Heimonen, J. S. Kottmann, T. Menke, W.-K. Mok, S. Sim, L.-C. Kwek, and A. Aspuru-Guzik, Noisy intermediate-scale quantum algorithms, *Rev. Mod. Phys.* **94**, 015004 (2022).
- [7] N. Cao, J. Lin, D. Kribs, Y.-T. Poon, B. Zeng, and R. Laflamme, NISQ: Error correction, mitigation, and noise simulation, *ArXiv:2111.02345* (2021).
- [8] S. Endo, Z. Cai, S. C. Benjamin, and X. Yuan, Hybrid quantum-classical algorithms and quantum error mitigation, *J. Phys. Soc. Jpn.* **90**, 032001 (2021).
- [9] A. Kandala, K. X. Wei, S. Srinivasan, E. Magesan, S. Carnevale, G. A. Keefe, D. Klaus, O. Dial, and D. C. McKay, Demonstration of a High-Fidelity CNOT Gate for Fixed-Frequency Transmons with Engineered ZZ Suppression, *Phys. Rev. Lett.* **127**, 130501 (2021).
- [10] H. Zhang, S. Chakram, T. Roy, N. Earnest, Y. Lu, Z. Huang, D. K. Weiss, J. Koch, and D. I. Schuster, Universal Fast-Flux Control of a Coherent, Low-Frequency Qubit, *Phys. Rev. X* **11**, 011010 (2021).
- [11] A. Somoroff, Q. Ficheux, R. A. Mencia, H. Xiong, R. V. Kuzmin, and V. E. Manucharyan, Millisecond coherence in a superconducting qubit, *ArXiv:2103.08578* (2021).
- [12] A. Gyenis, P. S. Mundada, A. Di Paolo, T. M. Hazard, X. You, D. I. Schuster, J. Koch, A. Blais, and A. A. Houck, Experimental Realization of a Protected Superconducting Circuit Derived from the $0-\pi$ Qubit, *PRX Quantum* **2**, 010339 (2021).
- [13] N. Ofek, A. Petrenko, R. Heeres, P. Reinhold, Z. Leghtas, B. Vlastakis, Y. Liu, L. Frunzio, S. M. Girvin, L. Jiang, M. Mirrahimi, M. H. Devoret, and R. J. Schoelkopf, Extending the lifetime of a quantum bit with error correction in superconducting circuits, *Nature* **536**, 441 (2016).
- [14] A. Grimm, N. E. Frattini, S. Puri, S. O. Mundhada, S. Touzard, M. Mirrahimi, S. M. Girvin, S. Shankar, and M. H. Devoret, Stabilization and operation of a Kerr-cat qubit, *Nature* **584**, 205 (2020).
- [15] W. D. Oliver and P. B. Welander, Materials in superconducting quantum bits, *MRS Bull.* **38**, 816 (2013).
- [16] A. P. M. Place, *et al.*, New material platform for superconducting transmon qubits with coherence times exceeding 0.3 milliseconds, *Nat. Commun.* **12**, 1779 (2021).
- [17] N. P. de Leon, K. M. Itoh, D. Kim, K. K. Mehta, T. E. Northup, H. Paik, B. S. Palmer, N. Samarth, S. Sangtawesin, and D. W. Steuerman, Materials challenges and opportunities for quantum computing hardware, *Science* **372**, eabb2823 (2021).
- [18] R. W. Simmonds, K. M. Lang, D. A. Hite, S. Nam, D. P. Pappas, and J. M. Martinis, Decoherence in Josephson Phase Qubits from Junction Resonators, *Phys. Rev. Lett.* **93**, 077003 (2004).
- [19] J. M. Martinis, K. B. Cooper, R. McDermott, M. Steffen, M. Ansmann, K. D. Osborn, K. Cicak, S. Oh, D. P. Pappas, R. W. Simmonds, and C. C. Yu, Decoherence in Josephson Qubits from Dielectric Loss, *Phys. Rev. Lett.* **95**, 210503 (2005).
- [20] I. Martin, L. Bulaevskii, and A. Shnirman, Tunneling Spectroscopy of Two-Level Systems Inside a Josephson Junction, *Phys. Rev. Lett.* **95**, 127002 (2005).
- [21] A. Lupaşcu, P. Bertet, E. F. C. Driessen, C. J. P. M. Harman, and J. E. Mooij, One- and two-photon spectroscopy of a flux qubit coupled to a microscopic defect, *Phys. Rev. B* **80**, 172506 (2009).
- [22] G. J. Grabovskij, T. Peichl, J. Lisenfeld, G. Weiss, and A. V. Ustinov, Strain tuning of individual atomic tunneling systems detected by a superconducting qubit, *Science* **338**, 232 (2012).
- [23] R. Barends, J. Kelly, A. Megrant, D. Sank, E. Jeffrey, Y. Chen, Y. Yin, B. Chiaro, J. Mutus, C. Neill, P. O'Malley, P. Roushan, J. Wenner, T. C. White, A. N. Cleland, and J. M. Martinis, Coherent Josephson Qubit Suitable for Scalable Quantum Integrated Circuits, *Phys. Rev. Lett.* **111**, 080502 (2013).
- [24] C. Wang, C. Axline, Y. Y. Gao, T. Brecht, Y. Chu, L. Frunzio, M. H. Devoret, and R. J. Schoelkopf, Surface participation and dielectric loss in superconducting qubits, *Appl. Phys. Lett.* **107**, 162601 (2015).
- [25] P. V. Klimov, *et al.*, Fluctuations of Energy-Relaxation Times in Superconducting Qubits, *Phys. Rev. Lett.* **121**, 090502 (2018).
- [26] J. J. Burnett, A. Bengtsson, M. Scigliuzzo, D. Niepce, M. Kudra, P. Delsing, and J. Bylander, Decoherence benchmarking of superconducting qubits, *npj Quantum Inf.* **5**, 54 (2019).
- [27] C. Müller, J. H. Cole, and J. Lisenfeld, Towards understanding two-level-systems in amorphous solids: Insights from quantum circuits, *Rep. Progr. Phys.* **82**, 124501 (2019).
- [28] J. Lisenfeld, A. Bilmes, S. Matityahu, S. Zanker, M. Marthaler, M. Schechter, G. Schön, A. Shnirman, G. Weiss, and A. V. Ustinov, Decoherence spectroscopy with individual two-level tunneling defects, *Sci. Rep.* **6**, 23786 (2016).
- [29] J. Lisenfeld, A. Bilmes, A. Megrant, R. Barends, J. Kelly, P. Klimov, G. Weiss, J. M. Martinis, and A. V. Ustinov, Electric field spectroscopy of material defects in transmon qubits, *npj Quantum Inf.* **5**, 105 (2019).
- [30] A. Bilmes, A. Megrant, P. Klimov, G. Weiss, J. M. Martinis, A. V. Ustinov, and J. Lisenfeld, Resolving the positions of defects in superconducting quantum bits, *Sci. Rep.* **10**, 3090 (2020).
- [31] A. Bilmes, S. Volosheniuk, J. D. Brehm, A. V. Ustinov, and J. Lisenfeld, Quantum sensors for microscopic tunneling systems, *npj Quantum Inf.* **7**, 27 (2021).
- [32] G. Andersson, A. L. O. Bilobran, M. Scigliuzzo, M. M. de Lima, J. H. Cole, and P. Delsing, Acoustic spectral hole-burning in a two-level system ensemble, *npj Quantum Inf.* **7**, 15 (2021).
- [33] A. Bilmes, S. Volosheniuk, A. V. Ustinov, and J. Lisenfeld, Probing defect densities at the edges and inside Josephson

- junctions of superconducting qubits, *npj Quantum Inf.* **8**, 24 (2022).
- [34] T. Yamamoto, Y. Nakamura, Y. A. Pashkin, O. Astafiev, and J. S. Tsai, Parity effect in superconducting aluminum single electron transistors with spatial gap profile controlled by film thickness, *Appl. Phys. Lett.* **88**, 212509 (2006).
- [35] S. Gustavsson, F. Yan, G. Catelani, J. Bylander, A. Kamal, J. Birenbaum, D. Hover, D. Rosenberg, G. Samach, A. P. Sears, S. J. Weber, J. L. Yoder, J. Clarke, A. J. Kerman, F. Yoshihara, Y. Nakamura, T. P. Orlando, and W. D. Oliver, Suppressing relaxation in superconducting qubits by quasiparticle pumping, *Science* **354**, 1573 (2016).
- [36] A. Hosseinkhani, R.-P. Riwar, R. J. Schoelkopf, L. I. Glazman, and G. Catelani, Optimal Configurations for Normal-Metal Traps in Transmon Qubits, *Phys. Rev. Appl.* **8**, 064028 (2017).
- [37] R.-P. Riwar and G. Catelani, Efficient quasiparticle traps with low dissipation through gap engineering, *Phys. Rev. B* **100**, 144514 (2019).
- [38] A. P. Vepsäläinen, A. H. Karamlou, J. L. Orrell, A. S. Dogra, B. Loer, F. Vasconcelos, D. K. Kim, A. J. Melville, B. M. Niedzielski, J. L. Yoder, S. Gustavsson, J. A. Formaggio, B. A. VanDevender, and W. D. Oliver, Impact of ionizing radiation on superconducting qubit coherence, *Nature* **584**, 551 (2020).
- [39] L. Cardani, *et al.*, Reducing the impact of radioactivity on quantum circuits in a deep-underground facility, *Nat. Commun.* **12**, 2733 (2021).
- [40] O. Rafferty, S. Patel, C. H. Liu, S. Abdullah, C. D. Wilen, D. C. Harrison, and R. McDermott, Spurious antenna modes of the transmon qubit, *ArXiv:2103.06803* (2021).
- [41] J. M. Martinis, Saving superconducting quantum processors from decay and correlated errors generated by gamma and cosmic rays, *npj Quantum Inf.* **7**, 90 (2021).
- [42] C. D. Wilen, S. Abdullah, N. A. Kurinsky, C. Stanford, L. Cardani, G. D'Imperio, C. Tomei, L. Faoro, L. B. Ioffe, C. H. Liu, A. Opremcak, B. G. Christensen, J. L. DuBois, and R. McDermott, Correlated charge noise and relaxation errors in superconducting qubits, *Nature* **594**, 369 (2021).
- [43] M. McEwen, *et al.*, Resolving catastrophic error bursts from cosmic rays in large arrays of superconducting qubits, *Nat. Phys.* **18**, 107 (2022).
- [44] E. T. Mannila, P. Samuelsson, S. Simbierowicz, J. T. Peltonen, V. Vesterinen, L. Grönberg, J. Hassel, V. F. Maisi, and J. P. Pekola, A superconductor free of quasiparticles for seconds, *Nat. Phys.* **18**, 145 (2022).
- [45] H. Wang, C. Shi, J. Hu, S. Han, C. C. Yu, and R. Q. Wu, Candidate Source of Flux Noise in SQUIDS: Adsorbed Oxygen Molecules, *Phys. Rev. Lett.* **115**, 077002 (2015).
- [46] P. Kumar, S. Sendelbach, M. A. Beck, J. W. Freeland, Z. Wang, H. Wang, C. C. Yu, R. Q. Wu, D. P. Pappas, and R. McDermott, Origin and Reduction of $1/f$ Magnetic Flux Noise in Superconducting Devices, *Phys. Rev. Appl.* **6**, 041001 (2016).
- [47] J. Goetz, F. Deppe, M. Haeberlein, F. Wulschner, C. W. Zollitsch, S. Meier, M. Fischer, P. Eder, E. Xie, K. G. Fedorov, E. P. Menzel, A. Marx, and R. Gross, Loss mechanisms in superconducting thin film microwave resonators, *J. Appl. Phys.* **119**, 015304 (2016).
- [48] M. V. P. Altoé, A. Banerjee, C. Berk, A. Hajr, A. Schwartzberg, C. Song, M. Alghadeer, S. Aloni, M. J. Elowson, J. M. Kreikebaum, E. K. Wong, S. M. Griffin, S. Rao, A. Weber-Bargioni, A. M. Minor, D. I. Santiago, S. Cabrini, I. Siddiqi, and D. F. Ogletree, Localization and Mitigation of Loss in Niobium Superconducting Circuits, *PRX Quantum* **3**, 020312 (2022).
- [49] M. Kudra, J. Biznárová, A. Fadavi Roudsari, J. J. Burnett, D. Niepce, S. Gasparinetti, B. Wickman, and P. Delsing, High quality three-dimensional aluminum microwave cavities, *Appl. Phys. Lett.* **117**, 070601 (2020).
- [50] A. Romanenko, R. Pilipenko, S. Zorzetti, D. Frolov, M. Awida, S. Belomestnykh, S. Posen, and A. Grassellino, Three-Dimensional Superconducting Resonators at $t < 20$ mK with Photon Lifetimes up to $\tau = 2$ s, *Phys. Rev. Appl.* **13**, 034032 (2020).
- [51] P. Heidler, C. M. F. Schneider, K. Kustura, C. Gonzalez-Ballester, O. Romero-Isart, and G. Kirchmair, Non-Markovian Effects of Two-Level Systems in a Niobium Coaxial Resonator with a Single-Photon Lifetime of 10 milliseconds, *Phys. Rev. Appl.* **16**, 034024 (2021).
- [52] J. Lisenfeld, C. Müller, J. H. Cole, P. Bushev, A. Lukashenko, A. Shnirman, and A. V. Ustinov, Rabi spectroscopy of a qubit-fluctuator system, *Phys. Rev. B* **81**, 100511(R) (2010).
- [53] S. Gustavsson, F. Yan, J. Bylander, F. Yoshihara, Y. Nakamura, T. P. Orlando, and W. D. Oliver, Dynamical Decoupling and Dephasing in Interacting Two-Level Systems, *Phys. Rev. Lett.* **109**, 010502 (2012).
- [54] S. Ashhab, J. Johansson, and F. Nori, Rabi oscillations in a qubit coupled to a quantum two-level system, *New J. Phys.* **8**, 103 (2006).
- [55] M. Carroll, S. Rosenblatt, P. Jurcevic, I. Lauer, and A. Kandala, Dynamics of superconducting qubit relaxation times, *npj Quantum Inf.* **8**, 132 (2022).
- [56] L. V. Abdurakhimov, I. Mahboob, H. Toida, K. Kakuyanagi, Y. Matsuzaki, and S. Saito, Driven-state relaxation of a coupled qubit-defect system in spin-locking measurements, *Phys. Rev. B* **102**, 100502(R) (2020).
- [57] F. Yan, S. Gustavsson, J. Bylander, X. Jin, F. Yoshihara, D. G. Cory, Y. Nakamura, T. P. Orlando, and W. D. Oliver, Rotating-frame relaxation as a noise spectrum analyser of a superconducting qubit undergoing driven evolution, *Nat. Commun.* **4**, 2337 (2013).
- [58] T. Van Duzer and C. Turner, *Principles of Superconductive Devices and Circuits* (Elsevier, New York, 1981).
- [59] A. Barone and G. Paterno, *Physics and Applications of the Josephson Effect* (Wiley, New York, 1982).
- [60] A. Schneider, T. Wolz, M. Pfirrmann, M. Spiecker, H. Rotzinger, A. V. Ustinov, and M. Weides, Transmon qubit in a magnetic field: Evolution of coherence and transition frequency, *Phys. Rev. Res.* **1**, 023003 (2019).
- [61] J. Krause, C. Dickel, E. Vaal, M. Vielmetter, J. Feng, R. Bounds, G. Catelani, J. M. Fink, and Y. Ando, Magnetic Field Resilience of Three-Dimensional Transmons with Thin-Film Al/AlO_x/Al Josephson Junctions Approaching 1 T, *Phys. Rev. Appl.* **17**, 034032 (2022).

- [62] P. Zhao, T. Ma, Y. Jin, and H. Yu, Combating fluctuations in relaxation times of fixed-frequency transmon qubits with microwave-dressed states, *Phys. Rev. A* **105**, 062605 (2022).
- [63] A. Galiatdinov, A. N. Korotkov, and J. M. Martinis, Resonator-zero-qubit architecture for superconducting qubits, *Phys. Rev. A* **85**, 042321 (2012).
- [64] Y. Matsuzaki and H. Nakano, Enhanced energy relaxation process of a quantum memory coupled to a superconducting qubit, *Phys. Rev. B* **86**, 184501 (2012).
- [65] M. Khezri, J. Dressel, and A. N. Korotkov, Qubit measurement error from coupling with a detuned neighbor in circuit QED, *Phys. Rev. A* **92**, 052306 (2015).
- [66] J. Q. You, X. Hu, S. Ashhab, and F. Nori, Low-decoherence flux qubit, *Phys. Rev. B* **75**, 140515(R) (2007).
- [67] M. Steffen, S. Kumar, D. P. DiVincenzo, J. R. Rozen, G. A. Keefe, M. B. Rothwell, and M. B. Ketchen, High-Coherence Hybrid Superconducting Qubit, *Phys. Rev. Lett.* **105**, 100502 (2010).
- [68] F. Yan, S. Gustavsson, A. Kamal, J. Birenbaum, A. P. Sears, D. Hover, T. J. Gudmundsen, D. Rosenberg, G. Samach, S. Weber, J. L. Yoder, T. P. Orlando, J. Clarke, A. J. Kerman, and W. D. Oliver, The flux qubit revisited to enhance coherence and reproducibility, *Nat. Commun.* **7**, 12964 (2016).
- [69] L. V. Abdurakhimov, I. Mahboob, H. Toida, K. Kakuyanagi, and S. Saito, A long-lived capacitively shunted flux qubit embedded in a 3D cavity, *Appl. Phys. Lett.* **115**, 262601 (2019).
- [70] J. Koch, T. M. Yu, J. Gambetta, A. A. Houck, D. I. Schuster, J. Majer, A. Blais, M. H. Devoret, S. M. Girvin, and R. J. Schoelkopf, Charge-insensitive qubit design derived from the Cooper pair box, *Phys. Rev. A* **76**, 042319 (2007).
- [71] L. Faoro, J. Bergli, B. L. Altshuler, and Y. M. Galperin, Models of Environment and T_1 Relaxation in Josephson Charge Qubits, *Phys. Rev. Lett.* **95**, 046805 (2005).
- [72] R. de Sousa, K. B. Whaley, T. Hecht, J. von Delft, and F. K. Wilhelm, Microscopic model of critical current noise in Josephson-junction qubits: Subgap resonances and Andreev bound states, *Phys. Rev. B* **80**, 094515 (2009).
- [73] L. Faoro and L. B. Ioffe, Microscopic origin of critical current fluctuations in large, small, and ultra-small area Josephson junctions, *Phys. Rev. B* **75**, 132505 (2007).
- [74] J. Johansson, P. Nation, and F. Nori, QuTiP: An open-source Python framework for the dynamics of open quantum systems, *Comput. Phys. Commun.* **183**, 1760 (2012).
- [75] J. Johansson, P. Nation, and F. Nori, QuTiP 2: A Python framework for the dynamics of open quantum systems, *Comput. Phys. Commun.* **184**, 1234 (2013).
- [76] A. F. Kockum, A. Miranowicz, V. Macrì, S. Savasta, and F. Nori, Deterministic quantum nonlinear optics with single atoms and virtual photons, *Phys. Rev. A* **95**, 063849 (2017).
- [77] P. Groszkowski and J. Koch, Scqubits: A Python package for superconducting qubits, *Quantum* **5**, 583 (2021).
- [78] D. Niepce, J. J. Burnett, M. Kudra, J. H. Cole, and J. Bylander, Stability of superconducting resonators: Motional narrowing and the role of Landau-Zener driving of two-level defects, *Sci. Adv.* **7**, eabh0462 (2021).
- [79] M. Spiecker, P. Paluch, N. Drucker, S. Matityahu, D. Gusenkova, N. Gosling, S. Günzler, D. Rieger, I. Takmakov, F. Valenti, P. Winkel, R. Gebauer, O. Sander, G. Catelani, A. Shnirman, A. V. Ustinov, W. Wernsdorfer, Y. Cohen, and I. M. Pop, A quantum Szilard engine for two-level systems coupled to a qubit, *ArXiv:2204.00499* (2022).
- [80] P. Aliferis, F. Brito, D. P. DiVincenzo, J. Preskill, M. Steffen, and B. M. Terhal, Fault-tolerant computing with biased-noise superconducting qubits: A case study, *New J. Phys.* **11**, 013061 (2009).
- [81] A. M. Stephens, W. J. Munro, and K. Nemoto, High-threshold topological quantum error correction against biased noise, *Phys. Rev. A* **88**, 060301(R) (2013).
- [82] D. K. Tuckett, S. D. Bartlett, and S. T. Flammia, Ultra-high Error Threshold for Surface Codes with Biased Noise, *Phys. Rev. Lett.* **120**, 050505 (2018).
- [83] D. K. Tuckett, A. S. Darmawan, C. T. Chubb, S. Bravyi, S. D. Bartlett, and S. T. Flammia, Tailoring Surface Codes for Highly Biased Noise, *Phys. Rev. X* **9**, 041031 (2019).
- [84] N. E. Frattini, U. Vool, S. Shankar, A. Narla, K. M. Sliwa, and M. H. Devoret, 3-wave mixing Josephson dipole element, *Appl. Phys. Lett.* **110**, 222603 (2017).
- [85] S. Kim, H. Terai, T. Yamashita, W. Qiu, T. Fuse, F. Yoshihara, S. Ashhab, K. Inomata, and K. Semba, Enhanced coherence of all-nitride superconducting qubits epitaxially grown on silicon substrate, *Commun. Mater.* **2**, 98 (2021).
- [86] S. Saito, X. Zhu, R. Amsüss, Y. Matsuzaki, K. Kakuyanagi, T. Shimo-Oka, N. Mizuochi, K. Nemoto, W. J. Munro, and K. Semba, Towards Realizing a Quantum Memory for a Superconducting Qubit: Storage and Retrieval of Quantum States, *Phys. Rev. Lett.* **111**, 107008 (2013).
- [87] A. Bienfait, J. J. Pla, Y. Kubo, X. Zhou, M. Stern, C. C. Lo, C. D. Weis, T. Schenkel, D. Vion, D. Esteve, J. J. L. Morton, and P. Bertet, Controlling spin relaxation with a cavity, *Nature* **531**, 74 (2016).
- [88] H. Toida, Y. Matsuzaki, K. Kakuyanagi, X. Zhu, W. J. Munro, H. Yamaguchi, and S. Saito, Electron paramagnetic resonance spectroscopy using a single artificial atom, *Commun. Phys.* **2**, 33 (2019).
- [89] V. Ranjan, J. O'Sullivan, E. Albertinale, B. Albanese, T. Chanelière, T. Schenkel, D. Vion, D. Esteve, E. Flurin, J. J. L. Morton, and P. Bertet, Multimode Storage of Quantum Microwave Fields in Electron Spins over 100 ms, *Phys. Rev. Lett.* **125**, 210505 (2020).
- [90] J. O'Sullivan, O. W. Kennedy, C. W. Zollitsch, M. Šėnas, C. N. Thomas, L. V. Abdurakhimov, S. Withington, and J. J. L. Morton, Spin-Resonance Linewidths of Bismuth Donors in Silicon Coupled to Planar Microresonators, *Phys. Rev. Appl.* **14**, 064050 (2020).